Evaluation of UTLS carbon monoxide simulations in GMI and GEOS-Chem chemical transport models using Aura MLS observations

Lei Huang[1], Jonathan H. Jiang[1], Lee T. Murray[2,3], Megan R. Damon[4], Hui Su[1], Nathaniel J. Livesey[1]

[1] {Jet Propulsion Laboratory, California Institute of Technology, Pasadena, CA}

[2] {NASA Goddard Institute for Space Studies, New York, NY}

[3] {Lamont-Doherty Earth Observatory, Columbia University, Palisades, NY}

[4] {NASA Goddard Space Flight Center, Greenbelt, MD}

Correspondence to: Lei Huang (Lei.Huang@jpl.nasa.gov)

Abstract

This study evaluates the distribution and variation of carbon monoxide (CO) in the upper troposphere and lower stratosphere (UTLS) during 2004–2012 as simulated by two chemical transport models, using the latest version of Aura Microwave Limb Sounder (MLS) observations. The simulated spatial distributions, temporal variations and vertical transport of CO in the UTLS region are compared with those observed by MLS. We also investigate the impact of surface emissions and deep convection on CO concentrations in the UTLS over different regions, using both model simulations and MLS observations. Global Modeling Initiative (GMI) and GEOS-Chem simulations of UTLS CO both show similar spatial distributions to observations. The global mean CO values simulated by both models agree with MLS observations at 215hPa and 147 hPa, but are significantly underestimated by more than 40% at 100 hPa. In addition, the models underestimate the peak CO values by up to 70% at 100 hPa, 60% at 147 hPa, and 40% at 215hPa, with GEOS-Chem generally simulating more CO at 100 hPa and less CO at 215hPa than GMI. The seasonal distributions of CO simulated by both models are in better agreement with MLS in the Southern Hemisphere (SH) than in the Northern Hemisphere (NH), with disagreements between model and observations over enhanced CO regions such as southern Africa. The simulated vertical transport of CO shows better agreement with MLS in the tropics and the SH subtropics than the NH subtropics. We also examine regional variations in the relationships among surface CO emission, convection and UTLS CO concentrations. The two models exhibit emission-convection-CO relationships similar to those observed by MLS over the tropics and some regions with enhanced UTLS CO.

1 Introduction

Carbon monoxide (CO) plays important roles in atmospheric chemistry and radiation balance. In particular, it serves as the primary sink of the hydroxyl radical (OH) (Logan et al., 1981) and is an important tropospheric ozone (O_3) precursor (Daniel and Solomon, 1998). CO in the troposphere is mostly emitted from the surface as a byproduct of incomplete combustion of carbon-based fuels, and it has primary sources from fossil fuel and biomass burning as well as secondary sources from oxidation of methane and other hydrocarbons (Jacob, 1999; Shindell et al., 2006). CO can be rapidly uplifted into mid- and upper troposphere by convection, where it can be transported around the globe (Jiang et al. 2007). With a typical lifetime of 1–2 months in the troposphere, CO has been often used as a tracer for studying the transport of polluted air masses that originate in regions of biomass burning or fossil fuel combustion (e.g., Allen et al., 1996; Edwards et al., 2006, Huang et al., 2012).

Previous studies using both satellite observations and model simulations have shown that CO has strong seasonal and interannual variations in the upper troposphere and lower stratosphere (UTLS) (e.g., Schoeberl et al., 2006; Liu et al., 2007; Liu et al., 2010, 2013; Huang et al., 2012, 2014). Temporal variations of CO in the UTLS are affected by many factors, including surface emission and convection, each having different seasonal variations; as well as photochemistry and transport, which can affect CO concentrations either locally or across a long distance. Schoeberl et al. (2006) studied vertical transport of CO across UTLS by analyzing the “tape recorder” - the vertical and temporal variations of CO observed by the Aura Microwave Limb Sounder (MLS) during August 2004 to December 2005. Their study indicates that the CO “tape recorder” arises from

combined seasonal variations in both surface emissions and convective transport of CO into the upper troposphere (UT). These can be simulated by the Global Modeling Initiative (GMI) chemical transport model (CTM) forced by climatological emissions. Many other studies also have shown that convolved seasonality in surface emissions and deep convective activity jointly produce enhanced CO fluxes from the surface to the UT resulting in seasonal peaks of CO (e.g., Liu et al., 2007; Liu et al., 2010; Huang et al., 2012). Strong interannual variation of CO in the UT has been found to be mainly associated with intense drought-induced fires in Indonesia and South America during El Niño periods (Liu et al., 2013; Livesey et al., 2013; Huang et al., 2014).

Although both surface emissions and convective transport could influence the seasonal peaks of CO in the UTLS, the relative importance of each factor varies between regions. Liu et al. (2007) suggested that high CO concentrations in the tropical UT during boreal Spring are mainly caused by a number of intense convective events over Africa and the Amazon that transport large amounts of fire-generated CO to the tropical tropopause layer. Ricaud et al. (2007) found that the peak in CO at the tropopause over Africa during boreal Spring largely results from convective and large-scale horizontal transport pathways, regardless of source region. Further study by Huang et al. (2012) confirmed that the locations and seasonality of the UT CO maxima in the tropics were strongly correlated with the frequency of local convection over South America and Central Africa during 2007. However, Schoeberl et al. (2006), using model simulations, argued that the UT CO maximum mainly results from strong biomass burning in Indo-China. Gonzi and Palmer (2010) further found that the fractions of surface CO emissions transported to the UT are lower over Africa and South America than over

Indonesia during June to October 2006. Although the relationships among emissions, convection, dynamical transport and UTLS CO abundance have been investigated by some observational studies (e.g., Jiang et al., 2007; Huang et al., 2012; Livesey et al. 2013), it is still not clear whether models can reproduce these relationships.

The ability of global CTMs to capture the processes driving CO temporal and spatial variations needs to be evaluated with observations. However, most of the previous model evaluation studies have been limited to comparison with in-situ surface observations (e.g., Duncan et al., 2007), in-situ aircraft field campaigns with limited spatial and temporal coverage (e.g., Hudman et al., 2007; Fisher et al., 2015), and ground- or satellite-based remotely sensed total column or coarse resolution vertical profile data (e.g., Edwards et al., 2006; Gloudemans et al., 2006; De Laat et al., 2007; Naik et al., 2013; Zeng et al., 2015). There are also some model inversion studies on CO sources (e.g., Heald et al., 2004; Kopacz et al., 2009), including a few studies using vertical CO information from multiple satellite products (e.g., Kopacz et al., 2010). Shindell et al. (2006) evaluated seasonal and spatial distributions of surface CO in 26 global atmospheric chemistry models and found that these models generally underestimate extratropical CO concentration in the Northern Hemisphere, although they typically perform reasonably well elsewhere. Fisher et al. (2015) showed large variabilities in the ability of different models to reproduce the observed CO profiles, and more complex chemical mechanisms do not necessarily produce more accurate simulation of CO vertical gradients. Zeng et al. (2015) compared simulated CO to observations from ground-based total column measurements at selected Southern Hemisphere (SH) sites and found that accurate representation of biogenic emissions is critical to reproducing observed SH background

CO. Although total column comparisons provide an advantage over in-situ surface comparisons for model validation in the free troposphere, neither surface nor total column data were able to constrain the vertical structure of CO in the models. Since 2004, the MLS instrument aboard the Aura satellite has been providing vertical profile measurements of various trace gases (e.g., CO, H_2O, O_3) in the UTLS, which have been widely used for trace gas distribution and transport studies (e.g., Park et al., 2009; Liu at al., 2010, 2013; Randel et al., 2010; Huang et al, 2012, 2014; Randel and Jensen, 2013). For example, Park et al. (2009) studied the source and transport of CO in the Asian monsoon circulation by using chemistry transport model simulation and MLS observation. Randel et al. (2010) identified the transport of polluted air masses from the surface to the stratosphere during Asian monsoon season by using MLS observation of hydrogen cyanide (HCN). Liu et al. (2010) evaluated CO transport in the GEOS-Chem CTM driven by GEOS-4 and GEOS-5 assimilated meteorological fields and discussed the differences with MLS observations. Huang et al. (2012, 2014) developed a method to automate the identification of convective transport pathways of CO through a joint use of MLS and A-Train satellite measurements and applied this method to study factors affecting the seasonal and interannual variations of tropical UT CO.

This study aims to evaluate the CO concentration and its distribution and variation in the UTLS during 2004–2012 simulated by two state-of-the-art CTMs using the latest version (V4.2) of Aura MLS data. The two models we use are GMI and GEOS-Chem. We will investigate whether the models can reproduce the relationships between surface CO emissions, convection and UTLS CO concentration seen in proxy and direct observations. Section 2 introduces the Aura MLS data and model simulations used.

Section 3 compares model-simulated climatological seasonal distributions, monthly variations and tape recorder signal of CO in the UTLS with the MLS observations. Section 4 analyzes and discusses the discrepancies in CO in the UTLS over selected regions between the model simulations and MLS observations. Section 5 investigates the convolved impacts of CO emissions and convection on UTLS CO concentrations in both the satellite observation and model simulations. The main conclusions of this study are summarized and discussed in Section 6.

2 Data

2.1 Aura MLS Observations

The MLS instrument aboard the Aura satellite was launched on 15 July 2004. Aura has a sun-synchronous orbit at an altitude of 705 km, with equatorial crossing times at 1:45 a.m. and 1:45 p.m. local solar time and a 16-day repeat cycle. MLS makes measurements of atmospheric composition, temperature, humidity and cloud ice in the upper troposphere and stratosphere by measuring thermal microwave emissions from broad spectral bands with a limb-viewing geometry (Waters et al., 2006). An advantage of MLS is that its measurements can be obtained in the presence of ice clouds and aerosols that prevent measurements by shorter wavelength infrared, visible and ultraviolet techniques. MLS observes CO at 240 GHz, with a vertical resolution of ~5 km in the UTLS and horizontal resolutions of ~6 km and 500–600 km across- and along-track, respectively (Livesey et al., 2008). An earlier version of the MLS CO retrieval (V2.2) was biased high by a factor of two at 215 hPa, although the morphology was generally realistic (Livesey et al., 2008). In a later version (V3.3), the high positive bias at 215 hPa was removed, but the impact of deep clouds on CO obervations was considerably worse

(Livesey et al., 2011). The newest version (V4.2) of the MLS data (Livesey et al. 2015) was released in July 2015, reduces the cloud impacts seen in V3.3 while avoiding the biases associated with V2.2. Comparisons of UTLS CO between the new (V4.2) and previous (V3.3) versions are discussed in Appendix A (Figs. A1 and A2). Only thick clouds that are typically associated with deep-convective cores are observable by MLS (Wu et al., 2008), thus MLS cloud ice water content (IWC) has been used as a proxy of deep convection in previous studies (e.g., Jiang et al., 2011; Liu et al., 2013; Livesey et al. 2013). In this study, we use MLS V4.2 Level 2 CO and IWC data, screening the data using recommended procedures (Livesey et al., 2015). The lowest usable retrieval level for CO and IWC is 215 hPa, where the estimated single-measurement precisions are ~19 ppbv for CO and ~1.2 mg m^{-3} for IWC. The systematic uncertainty for CO at 215 hPa is ±30 ppbv and ±30%, and generally ±30% at other UTLS pressure levels (Livesey et al., 2015).

2.2 GMI and GEOS-Chem Model Simulations

2.2.1 GMI Model

The GMI is a global 3-D CTM that includes full chemistry for both the troposphere and stratosphere. The GMI model is an assessment tool as part of the NASA Modeling, Analysis, and Prediction (MAP) program. It is capable of multiyear simulations for assessments of anthropogenic impacts on atmospheric composition and the role of long-range transport of pollution (Rotman et al., 2001). The GMI model includes a combined stratosphere-troposphere chemical mechanism with 124 species, 320 chemical reactions, and 81 photolytic reactions. The chemical mechanism in the troposphere includes a detailed description of tropospheric ozone, NO_x, and hydrocarbon

171 photochemistry (Bey et al., 2001a). Photolysis rates in the troposphere and stratosphere
172 are calculated by using the Fast-JX radiative transfer algorithm (Wild et al., 2000; Bian
173 and Prather, 2002), which is an efficient algorithm for calculating photolysis rates in the
174 presence of clouds and aerosols. Radiative and heterogeneous effects of aerosols on
175 photochemistry are included in this model. Biogenic emissions of isoprene and
176 monoterpenes are calculated online (Guenther et al., 2006). Surface methane is read from
177 climatological monthly files, and allowed to advect and react. Convective transport of
178 trace gases is parameterized using a modified CONV_TRAN routine contained in the
179 NCAR CCM3 physics package (Kiehl et al., 1998).

180 The time period of the GMI hindcast simulation is 1990–2012, with 1990–1994
181 considered as the hindcast spinup period. Therefore, the GMI simulation used in this
182 analysis is for 2004 through 2012. The meteorological fields are from the Global
183 Modeling and Assimilation Office (GMAO) Modern-Era Retrospective Analysis for
184 Research and Applications (MERRA) reanalysis (Rienecker et al., 2011). The MERRA
185 data have 72 vertical levels with a top at 0.01 hPa, and the horizontal resolution is $1/2^\circ$
186 latitude $\times$ $2/3^\circ$ longitude, which has been degraded to 2° latitude $\times$ 2.5° longitude for
187 input to the CTM. The biomass burning (BB) emissions used in the simulation are from
188 the Global Fire Emission Database version 3 (GFED3) (van der Werf et al., 2010). The
189 fossil fuel (FF) emissions are based on the Emission Database for Global Atmospheric
190 Research (EDGAR) v3.2 inventory for 2000, overwritten with regional inventories over
191 specific regions (Zhang et al. (2009) inventory for 2006 over Asia, EPA NEI 2005 over
192 USA, EMEP over Europe, BRAVO over Mexico, CAC over Canada). The year-to-year
193 variability in the FF emissions is calculated wherever the inventories have year-specific

194 information. Otherwise, scaling factors from GEOS-Chem model (van Donkelaar et al.,
195 2008) are used to make the FF emissions year-specific. However, at the time when the
196 GMI emissions were generated, the GEOS-Chem scaling factors ended in 2006, so for
197 2007–2012, the USA emissions were scaled based on EPA emission totals for each year
198 and the European emissions were scaled on a country-wide basis using national emissions
199 from EMEP, and the Asian emissions were scaled using the REAS inventory projections.
200 Biofuel emissions are from Yevich and Logan (2003) and EPA emission inventory.

201 **2.2.2 GEOS-Chem Model**

202 GEOS-Chem is a global 3-D CTM developed by the atmospheric chemistry group at
203 Harvard University and has been widely used around the world. It is driven by
204 assimilated meteorological observations from the NASA GMAO Goddard Earth
205 Observing System (GEOS) (Bey et al., 2001b). GEOS-Chem includes a fully-coupled
206 treatment of tropospheric O_3-NO_x-VOC chemistry and various types of aerosols (e.g.,
207 Park et al., 2003; Alexander et al., 2005), along with 155 species, 292 chemical reactions,
208 and 64 photolytic reactions. Chemistry is fully resolved in the troposphere, with a
209 linearized scheme applied in the stratosphere (Murray et al., 2013). Emissions in
210 GEOS-Chem are from the same several basic inventories as used by GMI, with annual
211 scaling factors applied to account for trends. As for GMI, the Fast-JX radiative transfer
212 algorithm is used in GEOS-Chem. Anthropogenic non-methane volatile organic
213 compounds (NMVOCs) are emitted from the REanalysis of the TROpospheric chemical
214 composition (RETRO) inventory (Schultz et al., 2007), except for propane and ethane,
215 which follow Xiao et al. (2008). Biogenic NMVOC emissions follow the Model of
216 Emissions and GAses from Nature (MEGAN), which vary monthly with observations of

leaf area indices from satellite and hourly with temperature, radiation, and precipitation (Barkley et al., 2011). Surface methane is read from monthly mean distributions interpolated from NOAA flask observations, and allowed to advect and react. Convective transport in GEOS-Chem is computed from the convective mass fluxes in the meteorological archive, as described by Wu et al. (2007). In this study, we use the simulations of GEOS-Chem version 9-02 (www.geos-chem.org) driven by MERRA reanalysis, the same meteorological fields as the GMI simulations. Vertical resolution is degraded from that of the MERRA inputs above 78.5 hPa but maintained at the MERRA resolution below, resulting in 47 total layers. The simulation period is 2003–2012, with January 2003 to April 2004 discarded as initialization. The model output data have a horizontal resolution of 2° latitude $\times$ 2.5° longitude, and 47 vertical layers between the surface and 0.01 hPa.

2.2.3 Differences between GMI and GEOS-Chem

To highlight the differences between the GMI and GEOS-Chem model run, we summarize their major differences in Table 1. In addition, we calculate the annual mean values and interannual standard deviations of CO budget (including biofuel and fossil fuel emissions, biomass burning emissions, tropospheric chemical production, tropospheric methane oxidation, loss with tropospheric OH, and net transport from troposphere to stratosphere) for GMI and GEOS-Chem during the period 2004–2012, and the results are provided in Table 2. In general, CO emissions from fuel combustion and biomass burning are mostly the same, but the chemical production and loss rates of CO in the troposphere are quite different between the two models. Specifically, GEOS-Chem is 40%, 16% and 15% higher than GMI in tropospheric chemical production Of CO,

tropospheric CH4 oxidation and CO loss with tropospheric OH, respectively. For the net CO transport from troposphere to stratosphere, GEOS-Chem is ~9.5% larger than GMI.

2.2.4 Model/MLS Comparison Approach

Both the GMI and GEOS-Chem simulations were archived at monthly temporal resolution, with the same horizontal resolution. GEOS-Chem provides model output on model levels whose pressure varies in time, whereas GMI provides output at fixed pressure levels. To compare the simulated and observed CO profiles, we first aggregate the daily Aura MLS along-track CO profiles into $2°$ latitude $\times 2.5°$ longitude grid boxes, and calculate monthly averages of CO in each grid box. We then apply the MLS V4.20 CO averaging kernels and a priori profiles to each model's simulated CO profiles to take into consideration the vertical sensitivity of the MLS retrieval for a most consistent comparison (Livesey et al., 2015). In this process, the modelled CO profiles are interpolated to the 37 pressure levels of the MLS retrieval.

3 Global Comparison between Models and Observation

3.1 Seasonal Distributions of CO in the UTLS

The climatological seasonal distributions of CO at 215 hPa as observed by MLS and simulated by GMI and GEOS-Chem are shown in Figure 1 (the differences between model simulations and MLS observation are shown in Fig. S1). The seasonal average is calculated as the 8-year average from December 2004 to November 2012. In general, the locations of high CO are well simulated in GMI and GEOS-Chem versus the MLS observations, except over Africa. MLS indicates that local maxima occur over central Africa during DJF and southern Africa during SON (Huang et al., 2012), but the simulated maxima were over West Africa during both of these two seasons. The

simulated CO values by both models are smaller than MLS observations, with an underestimation of generally less than 20% for the global mean (80°S–80°N) CO concentration (Table 3a). The largest underestimation occurs in MAM and JJA for both models, with GMI (GEOS-Chem) showing 20% (22.1%) and 20.2% (19.5%) less mean CO in MAM and JJA than MLS observations, respectively. Furthermore, peaks of simulated CO concentrations are smaller than MLS observations by up to ~40% for all seasons. The trans-Pacific transport of CO from East Asia in MAM and JJA to North America is shown in the model simulations, but the CO concentrations are ~30% lower than the observations. Continental outflow of CO in the UT from the eastern US and West Africa to the Atlantic Ocean during JJA is also poorly simulated by both models. The simulated CO distribution of GMI is quite similar to that of GEOS-Chem (the correlation coefficient between the two maps for each season is greater than 0.98), with the difference of mean CO less than 7% (Table 3a). The mean and peak values of simulated CO in GEOS-Chem are generally less than those from GMI at this level, especially over South America and Africa during DJF and SON (CO peak in GEOS-Chem is ~20% less than that in GMI).

At 147 hPa, high CO concentrations are mainly found in the tropical and sub-tropical latitudes, especially over South America and Africa (Figs. 2 and S2). During boreal Summer, there is a broad maximum over South Asia driven by convection associated with the Asian Summer monsoon (Fu et al., 2006; Park et al. 2009; Randel et al., 2010). However, this maximum in model simulations is not as broad as in the MLS observations. In addition, both models underestimate CO concentrations poleward of 50°. The underestimation is generally less than 32% for the global mean CO concentration (Table

3b), with the largest underestimation occurring in MAM for both models (32.4% for GMI, 31.5% for GEOS-Chem). In addition, seasonal CO maxima are also underestimated by about 30–40% in the tropics. The difference in mean CO concentration between the two model simulations is generally less than 5%, with GEOS-Chem slightly larger than GMI during all seasons except DJF (Table 3b). Maxima over South America and West Africa during SON and DJF are greater in magnitude (~15%) in GMI than in GEOS-Chem, but the latter shows a greater maximum (~9%) over South Asia during JJA than the former. The largest model-observation discrepancies occur at 100 hPa as shown in Figure 3 (and Fig. S3). Both models significantly underestimate the observed CO concentrations (note the different color scales in Fig. 3) compared to MLS. The underestimation is larger than 40% for the global mean CO concentration (Table 3c), with the largest underestimation occurring in MAM for both models (47.8% for GMI, 44.8% for GEOS-Chem). Although the simulations generally capture the local maxima and minima in each season, the magnitudes are significantly smaller than the observation. The underestimation of CO extremes from GMI ranges from ~22% to ~70% compared with MLS CO, while the underestimation from GEOS-Chem ranges ~18–68%. Both model simulations show similar CO distributions to each other, but the CO maxima in GMI are generally smaller than those in GEOS-Chem, with a maximum difference of ~8.7% during JJA for the global mean CO (Table 3c).

The vertical distribution of zonal mean CO and its seasonal variations are shown in Figure 4 (and Fig. S4). In general, MLS CO shows a pipe-like maximum in the tropics from 200 hPa to 100 hPa, with a stronger vertical gradient above 100 hPa than below. However, the simulations have more diffuse horizontal gradients in the UT and the

vertical gradient of CO is stronger below 100 hPa and weaker above 100 hPa than MLS. This may suggest that upward transport of CO is underestimated in the models. The average model bias (model CO minus MLS CO and then divided by MLS CO, same hereinafter) is -24 ~ -27% for GMI and -23 ~ -24% for GEOS-Chem throughout the year. The maximum model bias is -64% for GMI and -63% for GEOS-Chem. Although the models successfully reproduce a seasonal shift of local UT maxima from the tropics to the northern subtropics from DJF to JJA, they fail to simulate the higher maxima in the southern subtropics during SON. This is mainly due to the underestimation of CO concentration in the UT over southern Africa and South America (Figs. 1 and 2). The two models' simulations are quite similar (correlation coefficient > 0.996), except some differences in magnitude below (i.e., at pressures greater than) 150 hPa during SON and DJF as previously shown in the CO distribution map (Fig. 1).

3.2 Monthly Variations of CO in the UTLS

The temporal variability of the zonal mean monthly CO from 30°S to 30°N at 215 hPa for more than 8 years (August 2004 – December 2012) is shown in Figure 5 (and Fig. S5). The high CO concentrations observed in the northern tropics and subtropics are underestimated in the models, especially from April to July when both models underestimate by as much as 33%, which is significant compared to the MLS measurement uncertainty. This is mainly due to the underestimated CO over South Asia and East Asia, as well as East US and downwind region as shown in Figure 1. As a consequence, the seasonal cycle of CO over this latitudinal band is not well simulated. The temporal variation of CO in the southern subtropics is well captured by GMI (r=0.83, n=15 latitudes × 101 months) and GEOS-Chem (r=0.80), except the magnitude is a little

smaller than observation (difference < 10%). High CO values simulated by GMI during ENSO periods are comparable with MLS CO (difference is 2% - 11%), which is mainly related to stronger CO emissions generated by drought-induced fires in Indonesia or South America compared to normal years (Liu et al., 2013; Livesey et al., 2013; Huang et al., 2014). The maximum model bias at this level is -34% for GMI and -33% for GEOS-Chem, while the mean model bias is -9% (GMI) and -14% (GEOS-Chem). GMI shows higher CO values in the tropics during DJF and SON than GEOS-Chem (difference is still within 10%), especially in some El Niño-Southern Oscillation (ENSO) years such as 2004-05, 2006-07 and 2010-11. The comparisons of zonal mean CO between MLS and models at 147 hPa are similar to 215 hPa (figure not shown). At 100 hPa (Figs. 6 and S6), the most distinctive feature is the semi-annual peaks with similar magnitudes in boreal Spring and Fall as shown in MLS data. This semi-annual variation of CO in the UT is mainly due to the temporal overlapping of surface biomass burning from different continents and the inter-hemispheric shifts of deep convection (Duncan et al., 2007; Liu et al., 2013). The two models significantly underestimate CO at this level, and the peak during MAM is much weaker than the other peak during SON. The model bias ranges -54% ~ -22% for GMI and -48% ~ -13% for GEOS-Chem. The semi-annual CO peaks during boreal Spring and Fall in GEOS-Chem are slightly (~5%) larger than those in GMI.

Figure 7 shows the temporal evolution of monthly meridional mean tropical (15°S–15°N) CO at 215 hPa (also see Fig. S7). In general, GMI shows better agreement with MLS observation than GEOS-Chem with respect to the locations and magnitudes of the high CO concentration, since the magnitudes of CO peaks are 14% weaker in

GEOS-Chem than in GMI. The correlation coefficients between observation and simulations are 0.78 and 0.81 for GMI and GEOS-Chem, respectively (n=144 longitudes × 101 months). The seasonal peaks over South America, Africa and Indonesia are well represented in the model simulations, but their magnitudes are smaller than those observed, especially over Africa and Indonesia (maximum bias is -42% for GMI and -51% for GEOS-Chem). The maxima (~160–170 ppbv) over Indonesia during 2006-07 El Niño are well captured by the models (difference between model and observation < 5%). At 147 hPa (figure not shown), the interannual variation of meridional mean CO is similar to that at 215 hPa, except that the seasonal high CO encompasses a larger zonal area. At 100 hPa, the consistency between the models and MLS is substantially worse, as indicated by the significant underestimation (> 50%) of CO peaks and the locations of seasonal CO maxima (Figs. 8 and S8). For example, MLS shows a local CO maximum (~90 ppbv) over Africa during November-December 2007 that the simulations do not capture. Furthermore, MLS detects clear semi-annual CO peaks over Africa, but the models only show one annual peak. The correlation coefficients between observation and simulations are also reduced to 0.74. Overall, the average magnitude of CO in GEOS-Chem is ~5% larger than that in GMI at this level.

3.3 CO "Tape Recorder"

Air masses can enter the stratosphere in the tropics, driven by adiabatic upwelling of the Brewer-Dobson circulation (Brewer, 1949). During this slow upward transport, seasonal and interannual variations in the mixing ratios of some trace gases are preserved, as first observed in water vapor by Mote et al. (1995). This phenomenon is termed the "tape recorder". Schoeberl et al. (2006) identified the CO tape recorder for the first time

using MLS observations from August 2004 to December 2005. In this study, we evaluate the model-simulated CO tape recorder by taking advantage of the multi-year MLS data now available. Figure 9 shows the CO tape recorder over the tropics (as a zonal mean between 15°S and 15°N). An 8-year mean (2005–2012) was subtracted from the monthly mean time series at each level for MLS data and the two models' simulations. The differences of CO tape recorder between MLS observation and model simulations are shown in Figure S9. In general, the observed and simulated CO tape recorders show good agreement (r=0.76 for GMI, r=0.81 for GEOS-Chem, n=11 levels × 101 months). The observations and simulations show a semi-annual cycle around 200 hPa and a strong annual cycle above 80 hPa. In the lower stratosphere, both models show that the tape recorder signal fades out at approximately the same altitude (~50 hPa or 20 km) and the phase lines are quite similar to MLS observations. In the upper troposphere, the two models simulate the interannual variation of CO during the Northern and Southern Hemisphere fire seasons, which suggests that the surface CO emissions account for most of the CO variation near the tropopause. The phase shift and CO anomaly magnitude in GMI simulation are more consistent with MLS observation than those in GEOS-Chem simulation. For example, the average difference of positive CO anomaly between GMI and MLS is 15%, while that for GEOS-Chem is 32%. The models show that the location of the "tape head" is near 200 hPa, which is in rough agreement with MLS. In addition, the strong positive CO anomalies during three ENSO years (2004-05, 2006-07 and 2010-11) are captured by both observation and models.

The CO tape recorder signal over northern subtropics (10–30°N) is shown in Figure 10 (also see Fig. S10). In general, model simulated tape recorders are not consistent with

observation, as shown by a 2-3 month time lag between the same phases of CO peak anomaly. This inconsistency may be caused by the underestimation of vertical transport in the models (Schoeberl et al., 2006; Liu et al., 2010). Over this region, the ENSO signal is not as strong in the MLS observations as that over the tropics, yet the two models still show high positive CO anomalies during several ENSO periods. For the southern subtropics (10–30 °S), MLS and models have much better agreement (Figs. 11 and S11). The seasonal peaks and phase shift of CO anomalies are well collocated between observation and simulations. GMI simulation is much closer to MLS observation than GEOS-Chem in magnitude. For example, the difference of positive CO anomaly between GMI and MLS is within 31%, while that for GEOS-Chem is within 48%. However, the magnitude of positive anomaly in GMI simulation is still smaller than MLS observation (except the 2006-07 El Niño year), which is mainly due to the underestimation of surface CO emission over South America and southern Africa (Liu et al., 2010, 2013).

4 Regional Comparison between Models and Observation

To further evaluate CO differences between observation and model simulations, we examine six regions of high CO: South America (0–30 °S, 40–80 °W), Southern Africa (0–30 °S, 10–40 °E), Northern Africa (0–30 °N, 15 °W–40 °E), East Asia (20–45 °N, 105–145 °E), South Asia (10–30 °N,70–105 °E), and Indonesia (10 °S–10 °N, 100–150 °E).

4.1 Monthly Variations of CO in the UTLS

Figure 12 shows the climatological monthly mean of CO at 215 hPa from MLS and the models over these regions. Both models underestimate the CO seen by the observations throughout the year over three regions (southern Africa, East Asia, and Indonesia). The largest underestimation for a month by GMI (GEOS-Chem) is 19% (33%)

424 over South America, 30% (36%) over southern Africa, 22% (23%) over northern Africa,
425 37% (35%) over East Asia, 31% (29%) over South Asia, and 22% (22%) over Indonesia.
426 The seasonal cycle of CO is similar between MLS and the models over South America
427 (r=0.81 for both models), southern Africa (r=0.74 for GMI, r=0.75 for GEOS-Chem), and
428 Indonesia (r=0.92 for GMI, r=0.95 for GEOS-Chem) (Figs. 12a, 12b, and 12f), although
429 the magnitudes are underestimated. Over these first two regions, MLS shows maxima in
430 October; both models greatly underestimate the peak value and fail to simulate the
431 observed decreasing trend from October to January. Over Indonesia, there is an average
432 underestimation of ~15% throughout the year. The underestimation of CO peaks over
433 these regions may be due to low biases in direct surface emission, the fraction of fire
434 emissions released above the boundary layer, biogenic NMVOC oxidation, and/or
435 upward convective transport. Over the other three regions, simulated seasonal variations
436 are not consistent with MLS. For example, MLS shows CO peaks in July for East Asia
437 and in August for South Asia (Figs. 12d and 12e), but the peaks in both models lag MLS
438 by one month. This is probably due to insufficient representation of vertical transport in
439 the CTMs or underlying meteorological reanalysis. CO mixing ratios simulated by GMI
440 are generally larger than by GEOS-Chem, with differences typically less than 10%.
441 However, the model differences are larger from October to February over South America
442 and Africa, with a maximum of ~20% (Figs. 12a-c).

443 At 147 hPa, the differences in CO are similar to those at 215 hPa (figure not shown).
444 Compared with MLS, the largest underestimation by GMI (GEOS-Chem) is 26% (32%)
445 over South America, 35% (35%) over southern Africa, 28% (27%) over northern Africa,
446 33% (32%) over East Asia, 28% (25%) over South Asia, and 19% (18%) over Indonesia.

The differences in CO at 100 hPa between MLS and the models are shown in Figure 13. The seasonal cycles are similar between MLS and models over South America, southern Africa and Indonesia (Figs. 13a, 13b and 13f), but large discrepancies exist over northern Africa and South Asia (Figs. 13c and 13e). The underestimation by the models reaches maximum at this level. For example, the largest underestimation by GMI is 46% over South America, 46% over southern Africa, 41% over northern Africa, 46% over East Asia, 42% over South Asia, and 36% over Indonesia, compared with MLS. In general, the temporal variations of GMI and GEOS-Chem are similar, but GMI is smaller than GEOS-Chem over all regions, especially from May to October.

4.2 Vertical Profiles of CO in the UTLS

To evaluate the vertical distribution of CO in the UTLS, we present 8-year seasonal mean CO profiles for each region (Fig. 14). Both models underestimate CO at all levels observed by MLS below (i.e., with pressures greater than) 50 hPa. The magnitude of underestimation depends on region, altitude and season. For instance, the difference between MLS and GMI CO during JJA increases monotonically from 215 hPa to 100 hPa over South America, whereas it first decreases (215 – 147 hPa) and then increases (147 – 100 hPa) over East Asia. This is also shown in earlier figures for the climatological monthly mean of CO in the UTLS (Figs. 12 and 13). In general, the differences between GMI and GEOS-Chem are largest at 215 hPa (up to 19%) during DJF, whereas the differences reach maximum at 100 hPa (up to 13%) during JJA. GMI mixing ratios are greater than GEOS-Chem at altitudes below (i.e., pressures greater than) 147 hPa over South America, Africa and Indonesia. However, it becomes slightly less than GEOS-Chem for heights above (i.e., pressures smaller than) 100 hPa. That the profile

shapes are different, despite identical underlying meteorology, suggests that the way in which each CTM parameterizes its convective transport (including detrainment and entrainment) is affecting the resulting vertical distribution.

5 Relation between Emission, Convection and UTLS CO

In the sections above, we have evaluated the spatial distributions and temporal variations of CO in the UTLS simulated by the two models, on both the global and regional scale. Previous studies have shown that CO in the upper troposphere can be affected by both surface emission and convection (e.g., Schoeberl et al., 2006; Liu et al., 2007; Liu et al., 2010; Huang et al., 2012), thus it is important to evaluate the abilities of models to simulate the relationships between surface emission, convection, and CO in the UTLS. In this way, we can better understand the differences between observation and simulation of CO in the UTLS.

The climatological monthly mean of surface CO emission from GMI (very similar to GEOS-Chem), IWC and CO at three pressure levels from MLS are shown in Figure 15. Each variable is normalized for comparison. MLS IWC is used here as a proxy of convective intensity ("CONV" in Fig. 15). In general, seasonality in CO at 147 hPa is similar to that at 215 hPa, but different from that at 100 hPa. The relationships between UTLS CO and emission and convection vary with regions. For example, over South America and southern Africa, the annual CO peak lags the emission peak by 1–2 months at 215 and 147 hPa. Over East and South Asia, the annual CO cycle closely follows the variation of convection at the two lower levels. Over northern Africa and Indonesia, it seems that both emission and convection are important in determining CO in the UTLS.

492 Due to the complexity of the emission-convection-CO relationship, we apply a
493 bi-variate composite analysis (Jiang et al., 2007), and the results are shown in Figures 16
494 and 17 for CO at 215 hPa over the tropics (30°S–30°N) and different regions,
495 respectively. The monthly mean CO mixing ratios at 215 hPa in each grid box from MLS
496 observation and model simulations are binned according to the total (anthropogenic and
497 biomass burning) surface CO emissions (x-axis) and the convective (CONV) index
498 (y-axis). The CONV index is calculated as the IWC (from MLS observation) or
499 convective mass flux (from two models' simulations) value in each grid box divided by
500 the regional mean value at the same level. We have compared MLS IWC with convective
501 mass flux from the models and found that they have good linear correlation (correlation
502 coefficients > 0.7, as shown in Fig. S12). The surface CO emission data used for GMI
503 simulation are reused for the MLS bi-variate composite analysis. The color contour
504 indicates the unity-based normalized CO value (i.e., 0 is the minimum and 1 is the
505 maximum) at each pressure level.
506 Over the tropics (Fig. 16), MLS shows that CO concentration at 215 hPa is high when
507 convection is strong. With the presence of deep convection (CONV > 1), CO generally
508 increases with increasing surface emission. When convection is relatively weak (CONV
509 < 0.1), CO is generally low and bears little connection with surface emission. CO
510 concentration reaches maximum when both convection and emission are strong. When
511 emission is very weak, the variation of CO may result from long-range transport
512 preceding convective lofting (Huang et al., 2012). For example, MLS shows a high CO
513 center when emission is relatively weak (between 0.02–0.1 g/m^2/month) and convection
514 is strong (CONV > 2), which is also captured in the GMI simulation, but not in the

GEOS-Chem simulation. In general, both GMI and GEOS-Chem simulations show similar emission-convection-CO relationships compared with MLS observation, except the slope of CO contours has some differences. For instance, GMI seems to overestimate CO when convection is moderate (0.05 < CONV < 1) or emission is strong (> 1 g/m^2/month), while GEOS-Chem underestimates CO when convection is strong (CONV > 1) with weak emission (< 0.1 g/m^2/month). At 147 hPa, the emission-convection-CO relationships are similar to those shown at 215 hPa. For MLS observations, CO increases with emission when convection is moderate or strong (CONV > 0.1), but the high CO when emission is weak with strong convection is more pronounced at 215 hPa than 147 hPa. The emission-convection-CO relationships simulated by GMI and GEOS-Chem also show similarity to MLS observation at 147 hPa, despite some differences in the slope of CO contours. At 100 hPa, the emission-convection-CO relationships simulated by the two models are quite different from MLS observation (figure not shown), probably due to the significantly underestimated convection and CO in the models at this level, thus we do not discuss them in detail here. For the regional discussion below, we will also only focus on 215 hPa and 147 hPa.

Over the six different regions (Fig. 17), MLS shows that CO concentrations at 215 hPa are generally high when emission and convection are strong. However, there are also distinct regional differences. Over South America, CO does not change much when convection is relatively weak (CONV < 1), even though strong emission is present. CO increases rapidly when emission is large (> 1 g/m^2/month) with strong convection. This suggests that local convection plays an important role in determining CO mixing ratio in the UT over this region, which has been demonstrated by previous studies (e.g., Huang et

al., 2012). Over southern and northern Africa, two high CO centers occur when convection is strong (CONV > 1), one is located in a weak emission regime (0.02–0.1 g/m^2/month), and the other is accompanied by strong emission (> 0.5 g/m^2/month). This is similar to the two CO centers at 215 hPa over the tropics (Fig. 16). It is noteworthy that there is a large CO difference between cases where emissions are 0.1 g/m^2/month and those with 0.5 g/m^2/month emissions over northern Africa, with the latter cases exhibiting larger CO. Over East and South Asia, CO concentration is high in all cases where deep convection is present (CONV > 1). Even when emission is weak (< 0.1 g/m^2/month), CO mixing ratio can still be high with strong convection, which suggests that CO transport by convection and advection may be important over this region. During the Asian Summer monsoon season, CO emitted from northeast India and southwest China can be transported by deep convection to the UTLS and trapped within the anticyclonic circulation (e.g., Li et al., 2005; Fu et al., 2006; Park et al. 2009). This may account for the high CO over these two regions even though local emission is relatively weak. Over Indonesia, MLS roughly shows two high CO centers, one occurs when both convection and emission are strong (upper right corner) and the other exists when strong emission with weak convection is present (lower right corner).

The emission-convection-CO relationships simulated by the two models are quite similar to each other, reflecting their underlying identical meteorology and similar emission inventories. When compared with MLS observation, there is similarity over some regions such as southern Africa, northern Africa and Indonesia. Over other regions, the observed and simulated relationships are quite different. For example, both GMI and GEOS-Chem show two CO centers when convection is strong (CONV > 1) over South

America, and they overestimate CO when convection is moderate (0.1 < CONV < 1). Over East Asia, both models overestimate CO when convection is weak or moderate, especially with weak emission (< 0.2 g/m^2/month). Over South Asia, both models show a high CO center when both convection and emission are weak (lower left corner), which is not seen in the MLS observation. The emission-convection-CO relationships at 147 hPa over different regions observed by MLS, and the comparisons between observation and model simulations are similar to those at 215 hPa, thus we will not discuss them in detail.

6 Conclusions

In this study, we evaluate the spatial distribution and temporal variation of CO in the upper troposphere and lower stratosphere (UTLS) during 2004–2012 simulated by two chemical transport models (GMI and GEOS-Chem) using the latest version (V4.2) of Aura MLS data. The seasonal and monthly variations of CO, as well as the transport of CO in the UTLS (the "tape recorder") are compared between MLS observations and model simulations, over both global and regional scales. In addition, the relationships between emission, convection, and CO mixing ratio in the UTLS are investigated over different regions using MLS observations and model simulations.

In general, the simulated CO distribution from GMI is quite similar to that from GEOS-Chem at all levels. However, the CO peak values of GEOS-Chem are ~15-20% smaller than GMI at 215 hPa and 147 hPa over South America and Africa during DJF and SON, and ~20% larger than GMI at 100 hPa over South Asia during JJA. Compared with MLS observation, the locations of high CO centers at 215 hPa and 147 hPa are well simulated in GMI and GEOS-Chem, except over Africa. The UTLS transport of CO from East Asia across the Pacific to North America in MAM and JJA is shown in the two

584 models' simulations, but the CO concentrations are much lower than those observed by
585 MLS. In addition, the magnitudes of simulated CO peaks are much smaller than MLS
586 observation, with a maximum underestimation of ~40% at 215 hPa, 50–60% at 147 hPa,
587 and ~70% at 100 hPa. For the vertical distribution of zonally averaged CO, the model
588 simulations show more diffuse UT horizontal gradients, stronger vertical gradients below
589 100 hPa and weaker gradients above 100 hPa than observed by MLS, which may be due
590 to the underestimated upward transport of CO. The two models successfully reproduce
591 the seasonal shift of CO centers in the UT from DJF to JJA, but they fail to simulate a
592 higher CO maximum in the southern subtropics during SON.

593 The high CO concentrations in the northern subtropics are largely underestimated in
594 the models from April to July, especially over South Asia and East Asia. By contrast, the
595 temporal variation of CO in the southern subtropics is well simulated by the models,
596 except that the magnitude is slightly smaller than observed. The high CO values in the
597 UT related to stronger CO emissions generated by drought-induced fires in Indonesia or
598 South America are well captured by GMI during ENSO periods. The semi-annual CO
599 peaks at 100 hPa are not well simulated by the two models, and the peak during MAM is
600 much weaker than the other peak during SON. In general, the observed and simulated CO
601 tape recorders show good agreement over the tropics and southern subtropics. The phase
602 shift and CO anomaly magnitude in the GMI simulation are more consistent with MLS
603 observation than those in the GEOS-Chem simulation. The models show that the location
604 of the tape head is near 200 hPa, which is in rough agreement with MLS data. Over the
605 northern subtropics, CO tape recorders simulated by the models show a 2-3 month time

606 lag between the same phases of CO peak anomaly, which may be caused by an
607 underestimation of vertical transport in the models.

608 On regional scales, the CO concentrations simulated by GMI are generally larger than
609 those from GEOS-Chem, with differences less than 10% at 215 hPa and 147 hPa. The
610 seasonal cycle of CO is similar between MLS and both models over South America,
611 southern Africa and Indonesia, although the magnitude greatly differs. Over three other
612 regions (northern Africa, East Asia, South Asia), the simulated seasonal variation of CO
613 is not consistent with MLS observation. At 100 hPa, GMI is smaller than GEOS-Chem
614 over all regions, especially from May to October. The underestimation of CO by the
615 models reaches its maximum at this level. Vertical CO profile comparisons show that the
616 models underestimate CO at all levels below (i.e., with pressures greater than) 50 hPa
617 observable by MLS, with the magnitude of underestimation depending on region, altitude
618 and season.

619 The relationships between emission, convection and UTLS CO vary with region.
620 Over the tropics, UT CO generally increases with increasing surface emission in the
621 presence of deep convection. When convection is relatively weak, UT CO is generally
622 low and changes little with surface emission. The maximum CO concentration occurs
623 when both convection and emission are strong. GMI and GEOS-Chem simulations
624 generally show similar emission-convection-CO relationships compared with MLS
625 observation at 215 hPa and 147 hPa, except the slope of CO contours have some
626 differences. At 100 hPa, the emission-convection-CO relationships simulated by the two
627 models are quite different from observations. On a regional scale, CO in the UT is
628 generally high when emission and convection are strong, but distinct regional differences

629 also exist, which may be associated with the relative importance of convection and
630 advection in CO transport over different regions. In addition, convection in the tropics
631 and mid-latitudes are fundamentally different, leading to differences in CO transport, and
632 the relative mix of CO from anthropogenic emission, biomass burning, and in-situ
633 production. The simulated emission-convection-CO relationships from GMI and
634 GEOS-Chem are similar to observation over some regions such as southern Africa,
635 northern Africa and Indonesia, but not all regions.

636 Overall, GMI and GEOS-Chem simulations of CO are similar given the same driving
637 meteorology and very similar emission inventories. However, model simulations still
638 show large discrepancies compared with MLS observations, especially in the lower
639 stratosphere, such as at 100 hPa. These discrepancies may be related to the convection
640 parameterization, inaccurate emission inventories, and chemical production and loss rate
641 of CO in the troposphere (e.g., Table 2). More efforts are needed to investigate these
642 factors to improve model simulations in future studies.

643

644 **Appendix A: Comparison of MLS Version 3 and Version 4 CO**

645 Our preliminary comparisons of MLS V3 and V4 CO data have shown that the spatial
646 distributions of CO in the UTLS are quite similar, except for some small differences in
647 the magnitude. In general, CO concentration differences between these two versions are
648 within 20%. The seasonal CO peak values of V4 are slightly larger than V3 at 215 hPa
649 and 147 hPa, but become smaller than V3 at 100 hPa. The maximum differences is ~12–
650 17% for different seasons.

651 The improvements of MLS V4 compared with V3 CO can be seen in the vertical
652 distribution of zonal mean CO (Fig. A1) and the vertical CO profiles (Fig. A2). One
653 improvement is that the cloud contamination is significantly reduced, the other is the
654 more realistic CO gradient from 215 hPa to 100 hPa. In order to better illustrate the
655 differences between different versions, we also add the CO measurements from the
656 Atmospheric Chemistry Experiment - Fourier Transform Spectrometer (ACE-FTS)
657 (Bernath et al., 2005). This instrument is on board the Canadian satellite SCISAT-1,
658 operating between 750 and 4400 cm^{-1} with a high spectral-resolution (0.02 cm^{-1}) and
659 using a solar occultation observation technique. ACE-FTS observations are used to derive
660 volume mixing ratio profiles of over 30 atmospheric trace gases (Boone et al., 2005),
661 measuring each spacecraft sunrise and sunset (~30 profiles per day compared to ~3500
662 for Aura MLS). It has been providing consistent measurements since February 2004. The
663 atmospheric profiles provided by ACE-FTS range in altitude of ~5–110 km depending on
664 the species, with a vertical resolution of ~3–4 km. The data used are ACE-FTS Level 2
665 Version 3.5 (V3.5) (Boone et al., 2013) with the same period as MLS data (August 2004
666 – December 2012).
667 The vertical distribution of zonal mean CO in the pressure-latitude cross-section and
668 its seasonal variations as observed by MLS and ACE-FTS are shown in Figure A1.
669 During boreal Winter (DJF), MLS V3 CO shows a decrease between 160 hPa and 130
670 hPa, which may be caused by cloud contamination. This abnormal gap does not exist in
671 MLS V4 and ACE-FTS CO observation. Such improvement is also shown during MAM.
672 In addition, the magnitude of high CO centers in MLS V4 is higher than that in MLS V3
673 and has better agreement with ACE-FTS measurement. The tropical average (30 °S–30 °N)

of CO vertical profile in the UTLS and its seasonal variation as observed by MLS and ACE-FTS are shown in Figure A2. Compared with MLS V3 data, V4 CO is slightly more realistic in the CO gradient from 215 hPa to 100 hPa. For example, MLS V3 data show that CO decreases from 215 hPa to 147 hPa and then increases from 147 hPa to 100 hPa during DJF season, but V4 data show that it monotonically decreases from 215 hPa to 100 hPa, which is consistent with ACE-FTS CO observation. This improvement is also found in regional analysis (e.g., Indonesia). Furthermore, MLS V4 CO also shows better agreement with ACE-FTS CO than V3 CO during other seasons.

Acknowledgements

This research is supported by the NASA Aura Science Team program. The study was performed at the Jet Propulsion Laboratory (JPL), California Institute of Technology, under contract with NASA. The first author would like to thank Dr. William G. Read for help with the application of MLS averaging kernels to model simulations, and thank Dr. Susan E. Strahan and Dr. Stephen D. Steenrod for helpful advice on GMI model data analysis. We appreciate the helpful comments from two anonymous reviewers that led to significant improvements of this paper.

References

Alexander, B., Savarino, J., Lee, C. C. W., Park, R. J., Jacob, D. J., Thiemens, M. H., Li, Q. B., and Yantosca, R. M.: Sulfate formation in sea-salt aerosols: Constraints from oxygen isotopes, J. Geophys. Res., 110, D10307, doi:10.1029/2004JD005659, 2005.

696 Allen, D. J., Kasibhatla, P., Thompson, A. M., Rood, R. B., Doddridge, B. G., Pickering,
697 K. E., Hudson, R. D., and Lin, S.: Transport-induced interannual variability of carbon
698 monoxide determined using a chemistry and transport model, J. Geophys. Res., 101,
699 28655–28669, 1996.
700 Barkley, M., P. Palmer, L. Ganzeveld, A. Arneth, D. Hagberg, T. Karl, A. Guenther, F.
701 Paulot, P. Wennberg, J. Mao, T. Kurosu, K. Chance, J.-F. Muller, I. De Smedt, M. Van
702 Roozendael, D. Chen, Y. Wang, and R. Yantosca: Can a "state of the art" chemistry
703 transport model simulate Amazonian tropospheric chemistry? , J. Geophys. Res., 116,
704 D16302, doi:10.1029/2011JD015893, 2011.
705 Bernath, P. F., McElroy, C. T., Abrams, M. C., Boone, C. D., Butler, M., Camy-Peyret,
706 C., Carleer, M., Clerbaux, C., Coheur, P.-F., Colin, R., DeCola, P., DeMazière, M.,
707 Drummond, J. R., Dufour, D., Evans,W. F. J., Fast, H., Fussen, D., Gilbert, K.,
708 Jennings, D. E., Llewellyn, E. J., Lowe, R. P., Mahieu, E., McConnell, J. C., McHugh,
709 M., McLeod, S. D., Michaud, R., Midwinter, C., Nassar, R., Nichitiu, F., Nowlan, C.,
710 Rinsland, C. P., Rochon, Y. J., Rowlands, N., Semeniuk, K., Simon, P., Skelton, R.,
711 Sloan, J. J., Soucy, M.-A., Strong, K., Tremblay, P., Turnbull, D., Walker, K.
712 A.,Walkty, I.,Wardle, D. A.,Wehrle, V., Zander, R., and Zou, J.: Atmospheric
713 Chemistry Experiment (ACE): Mission overview, Geophys. Res. Lett., 32, L15S01,
714 doi:10.1029/2005GL022386, 2005.
715 Bey, I., Aumont, B., and Toupance, G.: A modeling study of the nighttime radical
716 chemistry in the lower continental troposphere: 1. Development of a detailed chemical
717 mechanism including nighttime chemistry, J. Geophys. Res., 106(D9), 9959–9990,
718 doi:10.1029/2000JD900347, 2001a.

719 Bey, I., Jacob, D. J., Yantosca, R. M., Logan, J. A., Field, B. D., Fiore, A. M., Li, Q. B.,
720 Liu, H. G. Y., Mickley, L. J., and Schultz, M. G.: Global modeling of tropospheric
721 chemistry with assimilated meteorology: Model description and evaluation, J. Geophys.
722 Res., 106, 23073–23096, 2001b.
723 Bian, H., and Prather, M. J.: Fast-J2: Accurate Simulation of stratospheric photolysis in
724 global chemical models, J. Atmos. Chem., 41, 281–296, 2002.
725 Boone, C. D., Nassar, R., Walker, K. A., Rochon, Y., McLeod, S. D., Rinsland, C. P., and
726 Bernath, P. F.: Retrievals for the Atmospheric Chemistry Experiment
727 Fourier-Transform Spectrometer, Appl. Optics, 44, 7218–7231,
728 doi:10.1364/AO.44.007218, 2005.
729 Boone, C. D., Walker, K. A., and Bernath, P. F.: Version 3 Retrievals for the
730 Atmospheric Chemistry Experiment Fourier Transform Spectrometer (ACE-FTS), The
731 Atmospheric Chemistry Experiment ACE at 10: A Solar Occultation Anthology, A.
732 Deepak Publishing, Hampton, Virginia, USA, 103–127, 2013.
733 Brewer, A. W.: Evidence for a World Circulation Provided by the Measurements of
734 Helium and Water Vapour Distribution in the Stratosphere, Q. J. Roy. Meteor. Soc., 75,
735 351–363, 1949.
736 Daniel, J. S., and Solomon, S.: On the climate forcing of carbon monoxide, J. Geophys.
737 Res., 103, 13249–13260, 1998.
738 De Laat, A., Gloudemans, A., Aben, I., Krol, M., Meirink, J., van der Werf, G., and
739 Schrijver, H.: SCIAMACHY carbon monoxide total columns: statistical evaluation and
740 comparison with CTM results, J. Geophys. Res., 112, D12310,
741 doi:10.1029/2006JD008256, 2007.

742 Duncan, B. N., Strahan, S. E., Yoshida, Y., Steenrod, S. D., and Livesey, N.: Model study
743 of the cross-tropopause transport of biomass burning pollution, Atmos. Chem. Phys., 7,
744 3713–3736, doi:10.5194/acp-7-3713-2007, 2007.
745 Edwards, D. P., Emmons, L. K., Gille, J. C., Chu, A., Attie, J. L., Giglio, L., Wood, S. W.,
746 Haywood, J., Deeter, M. N., Massie, S. T., Ziskin, D. C., and Drummond, J. R.:
747 Satellite-observed pollution from Southern Hemisphere biomass burning, J. Geophys.
748 Res., 111, D14312, doi:10.1029/2005JD006655, 2006.
749 Fisher, J. A., Wilson, S. R., Zeng, G., Williams, J. E., Emmons, L. K., Langenfelds, R. L.,
750 Krummel, P. B., and Steele, L. P.: Seasonal changes in the tropospheric carbon
751 monoxide profile over the remote Southern Hemisphere evaluated using multi-model
752 simulations and aircraft observations, Atmos. Chem. Phys., 15, 3217-3239,
753 doi:10.5194/acp-15-3217-2015, 2015.
754 Fu, R., Hu, Y. L., Wright, J. S., Jiang, J. H., Dickinson, R. E., Chen, M. X., Filipiak, M.,
755 Read, W. G., Waters, J. W., and Wu, D. L.: Short circuit of water vapor and polluted
756 air to the global stratosphere by convective transport over the Tibetan Plateau, P. Natl.
757 Acad. Sci. USA, 103, 5664–5669, doi:10.1073/pnas.0601584103, 2006.
758 Gloudemans, A., Krol, M., Meirink, J., De Laat, A., Van der Werf, G., Schrijver, H., Van
759 den Broek, M., and Aben, I.: Evidence for long-range transport of carbon monoxide in
760 the Southern Hemisphere from SCIAMACHY observations, Geophys. Res. Lett., 33,
761 L16807, doi:10.1029/2006GL026804, 2006.
762 Gonzi, S., and Palmer, P. I.: Vertical transport of surface fire emissions observed from
763 space, J. Geophys. Res., 115, D02306, doi:10.1029/2009JD012053, 2010.

764 Guenther, A., Karl, T., Harley, P., Wiedinmyer, C., Palmer, P. I., and Geron, C.:
765 Estimates of global terrestrial isoprene emissions using MEGAN (Model of Emissions
766 of Gases and Aerosols from Nature), Atmos. Chem. Phys., 6, 3181–3210,
767 doi:10.5194/acp-6-3181-2006, 2006.
768 Heald, C. L., D. J. Jacob, D. B. A. Jones, P. I. Palmer, J. A. Logan, D. G. Streets, G. W.
769 Sachse, J. C. Gille, R. N. Hoffman, and T. Nehrkorn: Comparative inverse analysis of
770 satellite (MOPITT) and aircraft (TRACE-P) observations to estimate Asian sources of
771 carbon monoxide, J. Geophys. Res., 109, D23306, doi:10.1029/2004JD005185, 2004.
772 Huang, L., Fu, R., Jiang, J. H., Wright, J. S., and Luo, M.: Geographic and seasonal
773 distributions of CO transport pathways and their roles in determining CO centers in the
774 upper troposphere, Atmos. Chem. Phys., 12, 4683–4698,
775 doi:10.5194/acp-12-4683-2012, 2012.
776 Huang, L., Fu, R., and Jiang, J. H.: Impacts of fire emissions and transport pathways on
777 the interannual variation of CO in the tropical upper troposphere, Atmos. Chem. Phys.,
778 14, 4087-4099, doi:10.5194/acp-14-4087-2014, 2014.
779 Hudman, R. C., et al.: Surface and lightning sources of nitrogen oxides over the United
780 States: Magnitudes, chemical evolution, and outflow, J. Geophys. Res., 112, D12S05,
781 doi:10.1029/2006JD007912, 2007
782 Jacob, D. J., Introduction to Atmospheric Chemistry, Princeton University Press,
783 Princeton, New Jersey, USA, 1999.
784 Jiang, J. H., Livesey, N. J., Su, H., Neary, L., McConnell, J. C., and Richards, N. A. D.:
785 Connecting surface emissions, convective uplifting, and long-range transport of carbon

786 monoxide in the upper troposphere: New observations from the Aura Microwave Limb
787 Sounder, Geophys Res Lett, 34, Doi 10.1029/2007gl030638, 2007.
788 Jiang, J. H., Su, H., Zhai, C., Massie, S. T., Schoeberl, M. R., Colarco, P. R., Platnick, S.,
789 Gu, Y., and Liou, K.-N.: Influence of convection and aerosol pollution on ice cloud
790 particle effective radius, Atmos. Chem. Phys., 11, 457–463, doi:
791 10.5194/acp-11-457-2011, 2011.
792 Kiehl, J. T., Hack, J. J., Bonan, G. B., Boville, B. A., Williamson, D. L., and Rasch, P. J.:
793 The National Center for Atmospheric Research Community Climate Model: CCM3, J.
794 Clim., 11(6), 1131–1149, 1998.
795 Kopacz, M., D. J. Jacob, D. Henze, C. L. Heald, D. G. Streets, and Q. Zhang:
796 Comparison of adjoint and analytical Bayesian inversion methods for constraining
797 Asian sources of carbon monoxide using satellite (MOPITT) measurements of CO
798 columns, J. Geophys. Res., 114, D04305, doi:10.1029/2007JD009264, 2009.
799 Kopacz, M., Jacob, D. J., Fisher, J. A., Logan, J. A., Zhang, L., Megretskaia, I. A.,
800 Yantosca, R. M., Singh, K., Henze, D. K., Burrows, J. P., Buchwitz, M., Khlystova, I.,
801 McMillan, W. W., Gille, J. C., Edwards, D. P., Eldering, A., Thouret, V., and Nedelec,
802 P.: Global estimates of CO sources with high resolution by adjoint inversion of
803 multiple satellite datasets (MOPITT, AIRS, SCIAMACHY, TES), Atmos. Chem.
804 Phys., 10, 855-876, doi:10.5194/acp-10-855-2010, 2010.
805 Li, Q. B., Jiang, J. H., Wu, D. L., Read, W. G., Livesey, N. J., Waters, J. W., Zhang, Y. S.,
806 Wang, B., Filipiak, M. J., Davis, C. P., Turquety, S., Wu, S. L., Park, R. J., Yantosca,
807 R. M., and Jacob, D. J.: Convective outflow of South Asian pollution: A global CTM

808 simulation compared with EOS MLS observations, Geophys. Res. Lett., 32, L14826,
809 doi:10.1029/2005GL022762, 2005.
810 Liu, C. T., Zipser, E., Garrett, T., Jiang, J. H., and Su, H.: How do the water vapor and
811 carbon monoxide “tape recorders” start near the tropical tropopause?, Geophys Res
812 Lett, 34, doi: 10.1029/2006gl029234, 2007.
813 Liu, J., Logan, J. A., Jones, D. B. A., Livesey, N. J., Megretskaia, I., Carouge, C., and
814 Nedelec, P.: Analysis of CO in the tropical troposphere using Aura satellite data and
815 the GEOS-Chem model: insights into transport characteristics of the GEOS
816 meteorological products, Atmos Chem Phys, 10, 12207-12232, DOI
817 10.5194/acp-10-12207-2010, 2010.
818 Liu, J., Logan, J. A., Murray, L. T., Pumphrey, H. C., Schwartz, M. J., and
819 Megretskaia, I. A.: Transport analysis and source attribution of seasonal and
820 interannual variability of CO in the tropical upper troposphere and lower stratosphere,
821 Atmos. Chem. Phys., 13, 129–146, doi: 10.5194/acp-13-129-2013, 2013.
822 Livesey, N. J., Filipiak, M. J., Froidevaux, L., Read, W. G., Lambert, A., Santee, M. L.,
823 Jiang, J. H., Pumphrey, H. C., Waters, J. W., Cofield, R. E., Cuddy, D. T., Daffer, W.
824 H., Drouin, B. J., Fuller, R. A., Jarnot, R. F., Jiang, Y. B., Knosp, B. W., Li, Q. B.,
825 Perun, V. S., Schwartz, M. J., Snyder, W. V., Stek, P. C., Thurstans, R. P., Wagner, P.
826 A., Avery, M., Browell, E. V., Cammas, J. P., Christensen, L. E., Diskin, G. S., Gao, R.
827 S., Jost, H. J., Loewenstein, M., Lopez, J. D., Nedelec, P., Osterman, G. B., Sachse, G.
828 W., and Webster, C. R.: Validation of Aura Microwave Limb Sounder O-3 and CO
829 observations in the upper troposphere and lower stratosphere, J Geophys Res-Atmos,
830 113, Doi 10.1029/2007jd008805, 2008.

831 Livesey, N. J., Read, W. G., Froidevaux, L., Lambert, A., Manney, G. L.: EOS MLS
832 version 3.3 Level 2 data quality and description document, Jet Propulsion Laboratory,
833 California Institute of Technology, Pasadena, CA, 2011.
834 Livesey, N. J., Logan, J. A., Santee, M. L., Waters, J. W., Doherty, R. M., Read, W. G.,
835 Froidevaux, L., and Jiang, J. H.: Interrelated variations of O3, CO and deep convection
836 in the tropical/subtropical upper troposphere observed by the Aura Microwave Limb
837 Sounder (MLS) during 2004–2011, Atmos. Chem. Phys., 13, 579-598,
838 doi:10.5194/acp-13-579-2013, 2013.
839 Livesey, N. J., Read, W. G., Wagner, P. A., Froidevaux, L., Lambert, A., Manney, G. L.,
840 Millán, L., Pumphrey, H. C., Santee, M. L., Schwartz, M. J., Wang, S., Fuller, R. A.,
841 Jarnot, R. F., Knosp, B. W., and Martinez, E.: EOS MLS Version 4.2x Level 2 data
842 quality and description document, Jet Propulsion Laboratory, California Institute of
843 Technology, Pasadena, CA, 2015.
844 Logan, J. A., Prather, M. J., Wofsy, S. C., and McElroy, M. B.: Tropospheric chemistry:
845 A global perspective, J. Geophys. Res., 86, 7210–7254, 1981.
846 Mote, P. W., Rosenlof, K. H., Holton, J. R., Harwood, R. S., and Waters, J. W.: Seasonal
847 variations of water vapor in the tropical lower stratosphere, Geophys. Res. Lett., 22,
848 1093–1096, 1995.
849 Murray, L. T., Logan, J. A., and Jacob, D. J.: Interannual variability in tropical
850 tropospheric ozone and OH: the role of lightning, J. Geophys. Res., 118, 11468–11480,
851 doi:10.1002/jgrd.50857, 2013.
852 Naik, V., Voulgarakis, A., Fiore, A. M., Horowitz, L. W., Lamarque, J.-F., Lin, M.,
853 Prather, M. J., Young, P. J., Bergmann, D., Cameron-Smith, P. J., Cionni, I., Collins,

W. J., Dalsøren, S. B., Doherty, R., Eyring, V., Faluvegi, G., Folberth, G. A., Josse, B., Lee, Y. H., MacKenzie, I. A., Nagashima, T., van Noije, T. P. C., Plummer, D. A., Righi, M., Rumbold, S. T., Skeie, R., Shindell, D. T., Stevenson, D. S., Strode, S., Sudo, K., Szopa, S., and Zeng, G.: Preindustrial to present-day changes in tropospheric hydroxyl radical and methane lifetime from the Atmospheric Chemistry and Climate Model Intercomparison Project (ACCMIP), Atmos. Chem. Phys., 13, 5277-5298, doi:10.5194/acp-13-5277-2013, 2013.

Park, M., Randel, W. J., Emmons, L. K., and Livesey, N. J.: Transport pathways of carbon monoxide in the Asian summer monsoon diagnosed from Model of Ozone and Related Tracers (MOZART), J. Geophys. Res., 114, D08303, doi:10.1029/2008JD010621, 2009.

Park, R. J., Jacob, D. J., Chin, M., and Martin, R. V.: Sources of carbonaceous aerosols over the United States and implications for natural visibility, J. Geophys. Res., 108, 4355, doi:10.1029/2002JD003190, 2003.

Randel, W. J. and Jensen, E. J.: Physical processes in the tropical tropopause layer and their roles in a changing climate, Nat. Geosci., 6, 169–176, doi:10.1038/ngeo1733, 2013.

Randel, W. J., Park, M., Emmons, L., Kinnison, D., Bernath, P., Walker, K. A., Boone, C., and Pumphrey, H.: Asian monsoon transport of pollution to the stratosphere, Science, 328, 611–613, 2010.

Ricaud, P., Barret, B., Attié, J.-L., Motte, E., Le Flochmoën, E., Teyssèdre, H., Peuch, V.-H., Livesey, N., Lambert, A., and Pommereau, J.-P.: Impact of land convection on

876 troposphere-stratosphere exchange in the tropics, Atmos. Chem. Phys., 7, 5639–5657,
877 doi:10.5194/acp-7-5639-2007, 2007.
878 Rienecker, M. M., Suarez, M. J., Gelaro, R., Todling, R., Bacmeister, J., Liu, E.,
879 Bosilovich, M. G., Schubert, S. D., Takacs, L., Kim, G.-K., Bloom, S., Chen, J.,
880 Collins, D., Conaty, A., da Silva, A., Gu, W., Joiner, J., Koster, R. D., Lucchesi, R.,
881 Molod, A., Owens, T., Pawson, S., Pegion, P., Redder, C. R., Reichle, R., Robertson, F.
882 R., Ruddick, A. G., Sienkiewicz, M., and Woollen, J.: MERRA: NASA's Modern-Era
883 Retrospective Analysis for Research and Applications, J. Climate, 24, 3624–3648,
884 doi:10.1175/JCLI-D-11-00015.1, 2011.
885 Rotman, D. A., Tannahill J. R., Kinnison D. E., Connell, P. S., Bergmann, D., Proctor, D.,
886 Rodriguez, J. M., Lin, S. J., Rood, R. B., Prather, M. J., Rasch, P. J., Considine, D. B.,
887 Ramaroson, R., and Kawa, S. R.: Global Modeling Initiative assessment model: Model
888 description, integration, and testing of the transport shell, J. Geophys. Res., 106(D2),
889 1669–1691, doi:10.1029/2000JD900463, 2001.
890 Schoeberl, M. R., Duncan, B. N., Douglass, A. R., Waters, J., Livesey, N., Read, W., and
891 Filipiak, M.: The carbon monoxide tape recorder, Geophys. Res. Lett., 33, doi:
892 10.1029/2006gl026178, 2006.
893 Schultz, M., Rast, S., van het Bolscher, M., Pulles, T., Brand, R., Pereira, J., Mota, B.,
894 Spessa, A., Dalsøren, S., van Nojie, T., and Szopa, S.: Emission data sets and
895 methodologies for estimating emissions, RETRO project report D1-6, Hamburg,
896 available at: http://retro.enes.org/reports/D1-6_final.pdf, 26 February 2007.
897 Shindell, D., Faluvegi, G., Stevenson, D., Krol, M., Emmons, L., Lamarque, J.-F., Petron,
898 G., Dentener, F., Ellingsen, K., Schultz, M., Wild, O., Amann, M., Atherton, C. S.,

899 Bergmann, D. J., Bey, I., Butler, T., Cofala, J., Collins, W. J., Derwent, R. G., Doherty,
900 R. M.,Drevet, J., Eskes, H. J., Fiore, A. M., Gauss, M., Hauglustaine, D. A., Horowitz,
901 L. W., Isaksen, I. S. A., Lawrence, M. G., Montanaro, V., Müller, J.-F., Pitari, G.,
902 Prather, M. J., Pyle, J. A., Rast, S., Rodriguez, J. M., Sanderson, M. G., Savage, N. H.,
903 Strahan, S. E., Sudo, K., Szopa, S., Unger, N., van Noije, T. P. C., and Zeng, G.:
904 Multimodel simulations of carbon monoxide: Comparison with observations and
905 projected near-future changes, J. Geophys. Res., 111, D19306,
906 doi:10.1029/2006JD007100, 2006.
907 van der Werf, G. R., Randerson, J. T., Giglio, L., Collatz, G., Mu, M., Kasibhatla, P. S.,
908 Morton, D. C., DeFries, R., Jin, Y., and van Leeuwen, T. T.: Global fire emissions and
909 the contribution of deforestation, savanna, forest, agricultural, and peat fires (1997–
910 2009), Atmos. Chem. Phys, 10, 11,707–711,735, 2010.
911 van Donkelaar, A., Martin, R. V., Leaitch, W. R., Macdonald, A. M., Walker, T. W.,
912 Streets, D. G., Zhang, Q., Dunlea, E. J., Jimenez, J. L., Dibb, J. E., Huey, L. G., Weber,
913 R., and Andreae, M. O.: Analysis of aircraft and satellite measurements from the
914 Intercontinental Chemical Transport Experiment (INTEX-B) to quantify long-range
915 transport of East Asian sulfur to Canada, Atmos. Chem. Phys., 8, 2999-3014,
916 doi:10.5194/acp-8-2999-2008, 2008.
917 Waters, J.W., Froidevaux, L., Harwood, R. S., Jarnot, R. F., Pickett, H. M., Read, W. G.,
918 Siegel, P. H., Cofield, R. E., Filipiak, M. J., Flower, D. A., Holden, J. R., Lau, G. K.,
919 Livesey, N. J., Manney, G. L., Pumphrey, H. C., Santee, M. L., Wu, D. L., Cuddy, D.
920 T., Lay, R. R., Loo, M. S., Perun., V. S., Schwartz, M. J., Stek, P. C., Thurstans, R. P.,
921 Chandra, K. M., Chavez, M. C., Chen, G., Boyles, M. A., Chudasama, B. V., Dodge,

R., Fuller, R. A., Girard, M. A., Jiang, J. H., Jiang, Y., Knosp, B. W., LaBelle, R. C., Lam, J. C., Lee, K. A., Miller, D., Oswald, J. E., Patel, N. C., Pukala, D. M., Quintero, O., Scaff, D. M., Snyder, W. V., Tope, M. C.,Wagner, P. A., andWalch, M. J.: The Earth Observing System Microwave Limb Sounder (EOS MLS) on the Aura satellite, IEEE Trans. Geosci. Remote Sens., 44, 1075–1092, 2006.

Wild, O., Zhu, X., and Prather, M.: Fast-J: Accurate simulation of in- and below- cloud photolysis in tropospheric chemical models, J. Atmos. Chem., 37, 245–282, 2000.

Wu, D. L., Jiang, J. H., Read, W. G., Austin, R. T., David, C. P., Lambert, A., Stephens, G. L., Vane, D. G., and Waters, J. W.: Validation of Aura MLS cloud Ice Water Content (IWC) measurements, J. Geophys. Res., 113, D15S10, doi:10.1029/2007LD008931, 2008.

Wu, S., L. J. Mickley, D. J. Jacob, J. A. Logan, R. M. Yantosca, and D. Rind: Why are there large differences between models in global budgets of tropospheric ozone? J. Geophys. Res., 112, D05302, doi:10.1029/2006JD007801, 2007.

Xiao, Y., J. A. Logan, D. J. Jacob, R. C. Hudman, R. Yantosca, and D. R. Blake: Global budget of ethane and regional constraints on U.S. sources, J. Geophys. Res., 113, D21306, doi:10.1029/2007JD009415, 2008.

Yevich, R., and Logan, J. A.: An assessment of biofuel use and burning of agricultural waste in the developing world, Global Biogeochem. Cycles, 17, 1095, doi:10.1029/2002GB001952, 2003.

Zeng, G., Williams, J. E., Fisher, J. A., Emmons, L. K., Jones, N. B., Morgenstern, O., Robinson, J., Smale, D., Paton-Walsh, C., and Griffith, D. W. T.: Multi-model simulation of CO and HCHO in the Southern Hemisphere: comparison with

observations and impact of biogenic emissions, Atmos. Chem. Phys., 15, 7217-7245, doi:10.5194/acp-15-7217-2015, 2015.

Zhang, G. J., and McFarlane, N. A.: Sensitivity of climate simulations to the parameterization of cumulus convection in the Canadian Climate Centre general circulation model, Atmos. Ocean., 33, 407–446, 1995.

Zhang, Q., Streets, D. G., Carmichael, G. R., He, K. B., Huo, H., Kannari, A., Klimont, Z., Park, I. S., Reddy, S., Fu, J. S., Chen, D., Duan, L., Lei, Y., Wang, L. T., and Yao, Z. L.: Asian emissions in 2006 for the NASA INTEX-B mission, Atmos. Chem. Phys., 9, 5131-5153, doi:10.5194/acp-9-5131-2009, 2009.

Table Captions

Table 1. Differences between GMI model and GEOS-Chem model run.

Table 2. Annual mean and interannual standard deviation of CO budgets (biofuel and fossil fuel emissions, biomass burning emissions, tropospheric chemical production, tropospheric methane oxidation, loss with tropospheric OH, and net transport from troposphere to stratosphere) for GMI and GEOS-Chem during 2004 – 2012 (units in Tmol/year).

Table 3. Statistical comparison of model-simulated and MLS-observed (V4) CO at (a) 215 hPa, (b) 147 hPa, and (c) 100 hPa during each season.

Figure Captions

Fig. 1. Seasonal mean (DJF, MAM, JJA, and SON) distribution of CO mixing ratio at 215 hPa for December 2004 – November 2012 from: (top row) MLS V4 data; (middle

968 row) GMI model simulation with MLS averaging kernels (AKs) applied; (bottom row)
969 GEOS-Chem model simulation with MLS AKs applied.
970 **Fig. 2.** As in Fig. 1, but for CO mixing ratio at 147 hPa.
971 **Fig. 3.** As in Fig. 1, but for CO mixing ratio at 100 hPa.
972 **Fig. 4.** Vertical/latitudinal distribution of zonal mean CO mixing ratio during different
973 seasons (DJF, MAM, JJA, and SON) from: (top row) MLS V4 data; (middle row) GMI
974 model simulation with MLS AKs applied; (bottom row) GEOS-Chem model simulation
975 with MLS AKs applied.
976 **Fig. 5.** Monthly variation of zonal mean CO mixing ratio at 215 hPa for August 2004 –
977 December 2012 from: (top row) MLS V4 data; (middle row) GMI model simulation with
978 MLS AKs applied; (bottom row) GEOS-Chem model simulation with MLS AKs applied.
979 **Fig. 6.** As in Fig. 5, but for CO mixing ratio at 100 hPa.
980 **Fig. 7.** Monthly variation of meridional mean (15°S–15°N) CO mixing ratio at 215 hPa
981 for August 2004 – December 2012 from: (left) MLS V4 data; (middle) GMI model
982 simulation with MLS AKs applied; (right) GEOS-Chem model simulation with MLS
983 AKs applied.
984 **Fig. 8.** As in Fig. 7, but for CO mixing ratio at 100 hPa.
985 **Fig. 9.** Temporal variation of monthly mean CO deviations, zonally averaged over the
986 tropics (15°S–15°N), vertically from 200 hPa to 50 hPa for August 2004 – December
987 2012 from (top row) MLS V4 data; (middle row) GMI model simulation with MLS AKs
988 applied; (bottom row) GEOS-Chem model simulation with MLS AKs applied. An 8-year
989 mean (2005–2012) was subtracted from the monthly mean time series at each level for
990 MLS data and the two models' simulations.

Fig. 10. As in Fig. 9, but over the northern subtropics (10°–30°N).

Fig. 11. As in Fig. 9, but over the southern subtropics (10°–30°S).

Fig. 12. Climatological (8-year) monthly mean of CO mixing ratio at 215 hPa from MLS V4 data (black line), GMI model simulation with MLS AKs applied (red line), and GEOS-Chem model simulation with MLS AKs applied (blue line) over the selected six regions: (a) South America, (b) Southern Africa, (c) Northern Africa, (d) East Asia, (e) South Asia, and (f) Indonesia. The error bars indicate ±1 interannual standard deviation of the monthly mean CO from MLS observation and model simulations.

Fig. 13. As in Fig. 12, but for CO mixing ratio at 100 hPa.

Fig. 14. Climatological (8-year) seasonal mean vertical profile of CO mixing ratio from MLS V4 data (black line), GMI model simulation with MLS AKs applied (red line), and GEOS-Chem model simulation with MLS AKs applied (blue line) over the selected six regions: (top row) South America, (second row from top) Southern Africa, (third row from top) Northern Africa, (fourth row from top) East Asia, (fifth row from top) South Asia, and (bottom row) Indonesia.

Fig. 15. Climatological monthly mean of surface CO emission from GMI model (red line), ice water content (blue line) and CO mixing ratio (black line) at 215 hPa (left column), 147 hPa (middle column), and 100 hPa (left column) from MLS observation over six regions: (top row) South America, (second row from top) Southern Africa, (third row from top) Northern Africa, (fourth row from top) East Asia, (fifth row from top) South Asia, and (bottom row) Indonesia. Each variable is normalized for comparison.

Fig. 16. Contour plots of normalized CO mixing ratio at 215 hPa (top row) and 147 hPa (bottom row) over the tropics (30°S–30°N) from MLS observation (left column), GMI

model simulation (middle column), and GEOS-Chem model simulation (left column) binned according to the surface CO emission (x-axis) and convective index (y-axis) at the same pressure level. See text for more details.

Fig. 17. Contour plots of normalized CO mixing ratio at 215 hPa over six regions: (top row) South America, (second row from top) Southern Africa, (third row from top) Northern Africa, (fourth row from top) East Asia, (fifth row from top) South Asia, and (bottom row) Indonesia, from MLS observation (left column), GMI model simulation (middle column), and GEOS-Chem model simulation (left column) binned according to the surface CO emission (x-axis) and convective index (y-axis) at the same pressure level. See text for more details.

Fig. A1. Vertical distribution of zonal mean CO mixing ratio in the pressure-latitude cross-section during different seasons (DJF, MAM, JJA, and SON) from: (top row) MLS Version 3 CO data; (middle row) MLS Version 4 CO data; (bottom row) ACE-FTS CO data with MLS averaging kernels (AKs) applied.

Fig. A2. Climatological (8-year) seasonal mean vertical profile of CO mixing ratio from MLS Version 4 CO data (black line), MLS Version 3 CO data (gray line), and ACE-FTS CO data with MLS AKs applied (red line) over the tropics (30 °S–30 °N).

Tables

Table 1. Differences between GMI model and GEOS-Chem model run.

	GMI	GEOS-Chem
Spin-up period	1990-1994	January 2003 – April 2004
Vertical resolution	72 levels (~38 levels in the tropical troposphere)	47 levels (~38 levels in the tropical troposphere)
Number of species	124	155
Number of chemical reactions	320	292

Number of photolytic reactions	81	64
chemistry mechanism	combined stratosphere/troposphere chemical mechanism	fully resolved in the troposphere, a linearized scheme applied in the stratosphere
Convective Parameterization	NCAR convection scheme	Relaxed Arakawa-Schubert scheme

Table 2. Annual mean and interannual standard deviation of CO budgets (biofuel and fossil fuel emissions, biomass burning emissions, tropospheric chemical production, tropospheric methane oxidation, loss with tropospheric OH, and net transport from troposphere to stratosphere) for GMI and GEOS-Chem during 2004 – 2012 (units in Tmol/year).

Model		GMI	GEOS-Chem
biofuel + fossil fuel		20.6 ± 0.16	19.6 ± 0.29
biomass burning		11.9 ± 1.9	11.9 ± 2.0
tropospheric chemical production		42.3 ± 0.92	59.1 ± 0.77
	source from methane oxidation	30.3 ± 0.95	35.2 ± 0.42
loss with tropospheric OH		77.7 ± 2.1	89.1 ± 2.4
net transport to stratosphere		1.37 ± 0.49	1.50 ± 0.47

Table 3. Statistical comparison of model-simulated and MLS-observed (V4) CO at (a) 215 hPa, (b) 147 hPa, and (c) 100 hPa during each season.

Level	Season	Correlation			Model Biases (%)								
					Maximum difference			Minimum difference			Mean difference		
		GMI vs V4	GEOS vs V4	GMI vs GEOS	GMI-V4	GEOS-V4	GEOS - GMI	GMI-V4	GEOS-V4	GEOS - GMI	GMI-V4	GEOS-V4	GEOS - GMI
(a) 215 hPa	DJF	0.89	0.90	0.990	-39.0	-40.8	-21.4	30.7	14.5	3.2	-10.5	-16.6	-6.8
	MAM	0.90	0.90	0.995	-36.6	-37.9	-12.1	7.50	4.1	4.1	-20.0	-22.1	-2.7
	JJA	0.83	0.85	0.993	-40.3	-39.9	-6.8	13.7	9.9	8.9	-20.2	-19.5	0.8
	SON	0.85	0.82	0.983	-43.5	-47.9	-19.9	44.3	45.1	4.3	-11.1	-14.5	-3.8
(b) 147 hPa	DJF	0.92	0.93	0.996	-61.7	-60.0	-17.4	6.4	-2.1	5.6	-27.5	-29.1	-2.2
	MAM	0.96	0.95	0.998	-59.7	-59.2	-7.0	-6.6	-5.5	6.5	-32.4	-31.5	1.3
	JJA	0.96	0.97	0.997	-53.8	-52.0	-1.9	-4.4	-5.6	15.6	-31.3	-27.8	5.2
	SON	0.96	0.96	0.996	-50.0	-47.9	-13.7	5.0	6.2	10.3	-25.2	-24.1	1.4
(c) 100 hPa	DJF	0.93	0.94	0.999	-70.2	-68.4	-3.2	-21.9	-21.9	8.4	-46.1	-43.9	4.0
	MAM	0.97	0.97	0.999	-64.1	-63.0	1.0	-29.8	-27.1	10.0	-47.8	-44.8	5.6
	JJA	0.92	0.93	0.998	-67.9	-66.4	1.4	-23.7	-18.6	20.1	-47.4	-42.8	8.7
	SON	0.97	0.97	0.997	-61.7	-60.0	-0.6	-22.0	-18.0	14.6	-44.7	-40.6	7.5

1044

Figures

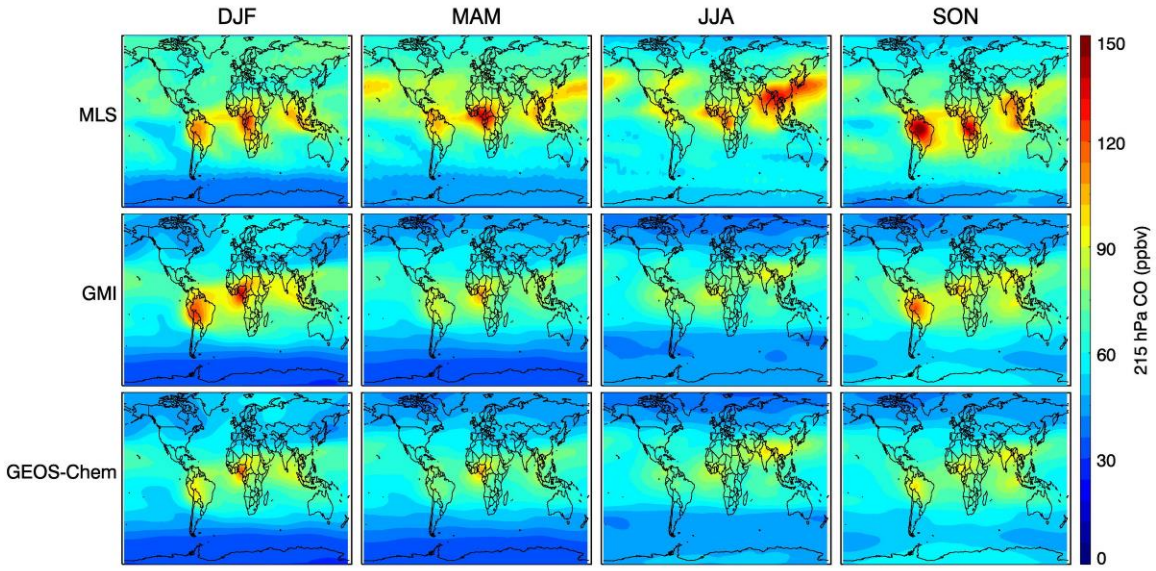

Fig. 1. Seasonal mean (DJF, MAM, JJA, and SON) distribution of CO mixing ratio at 215 hPa for December 2004 – November 2012 from: (top row) MLS V4 data; (middle row) GMI model simulation with MLS averaging kernels (AKs) applied; (bottom row) GEOS-Chem model simulation with MLS AKs applied.

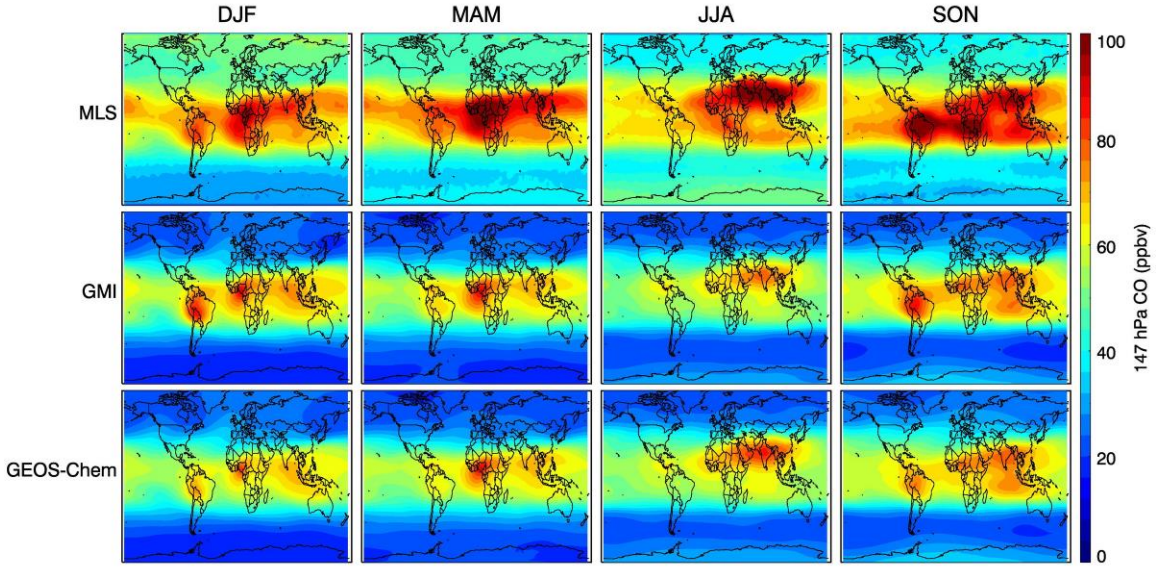

Fig. 2. As in Fig. 1, but for CO mixing ratio at 147 hPa.

1053

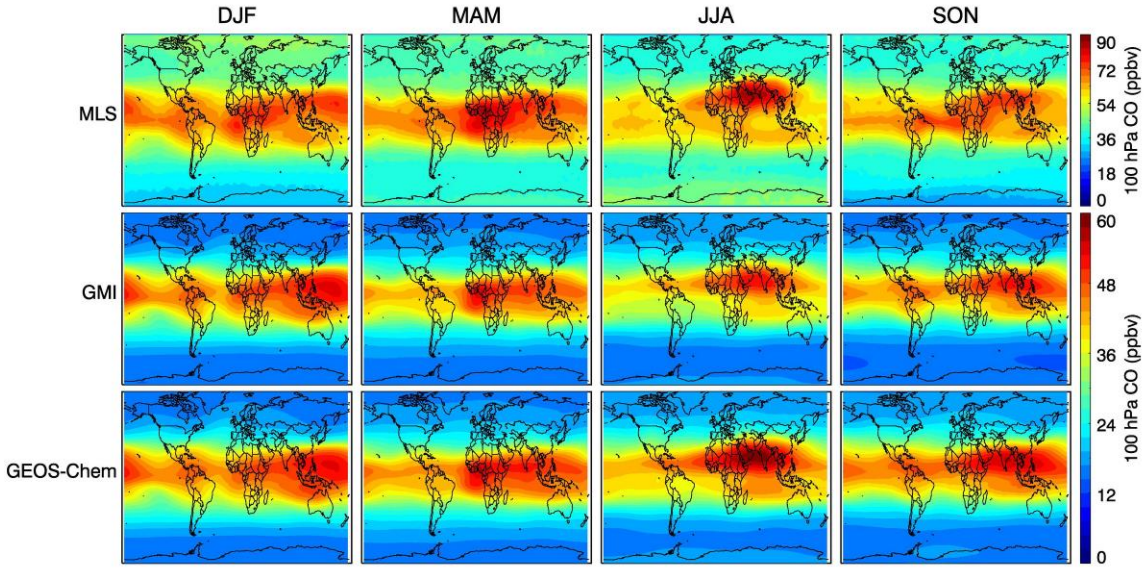

1054

1055 **Fig. 3.** As in Fig. 1, but for CO mixing ratio at 100 hPa.

1056

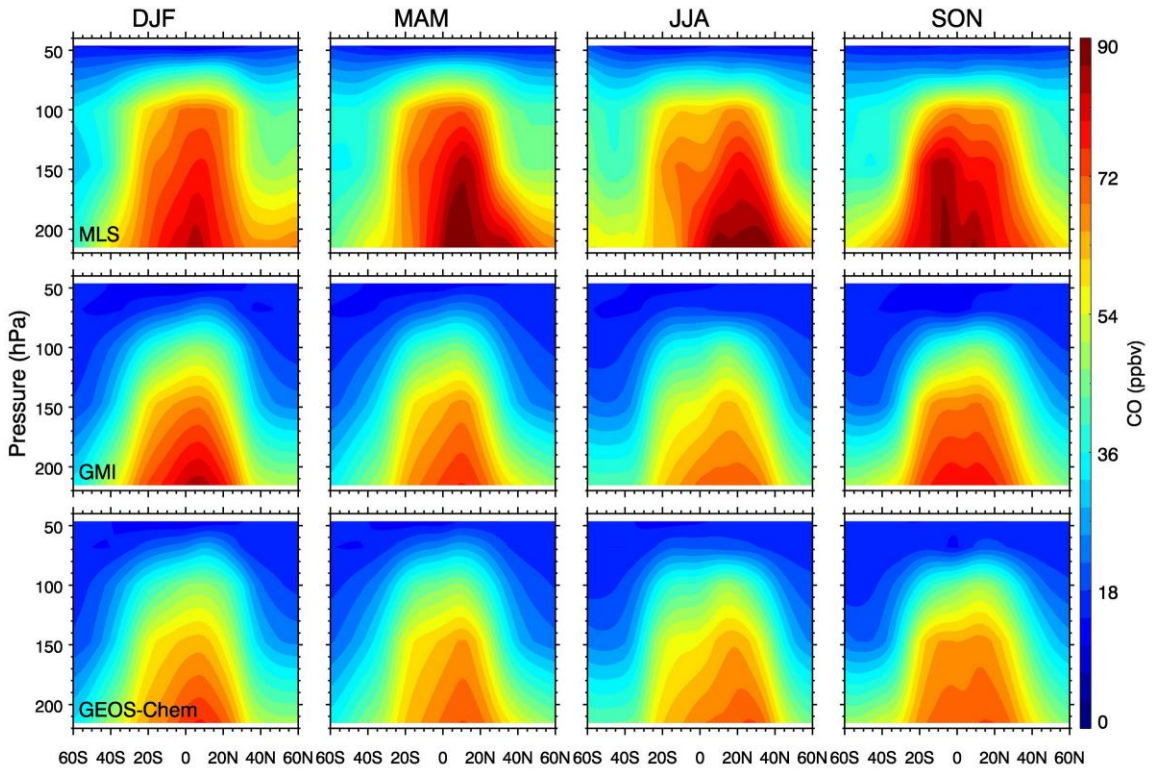

Fig. 4. Vertical/latitudinal distribution of zonal mean CO mixing ratio during different seasons (DJF, MAM, JJA, and SON) from: (top row) MLS V4 data; (middle row) GMI model simulation with MLS AKs applied; (bottom row) GEOS-Chem model simulation with MLS AKs applied.

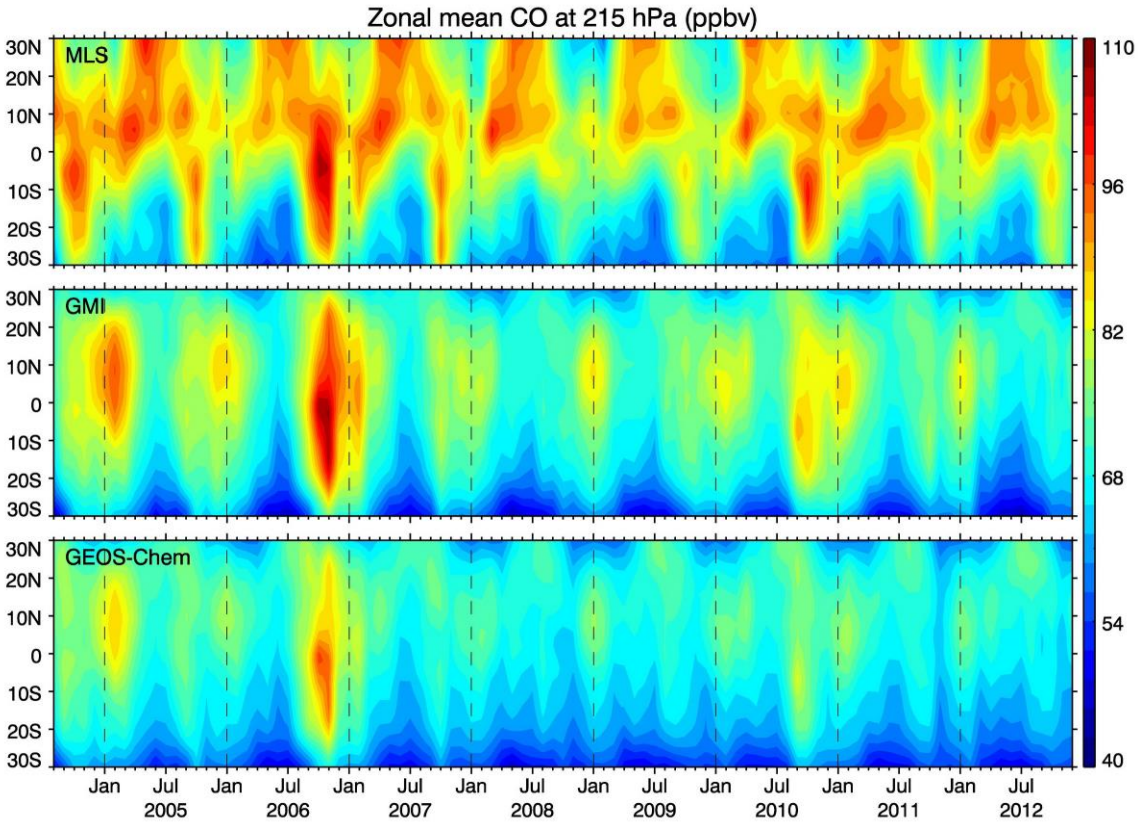

Fig. 5. Monthly variation of zonal mean CO mixing ratio at 215 hPa for August 2004 – December 2012 from: (top row) MLS V4 data; (middle row) GMI model simulation with MLS AKs applied; (bottom row) GEOS-Chem model simulation with MLS AKs applied.

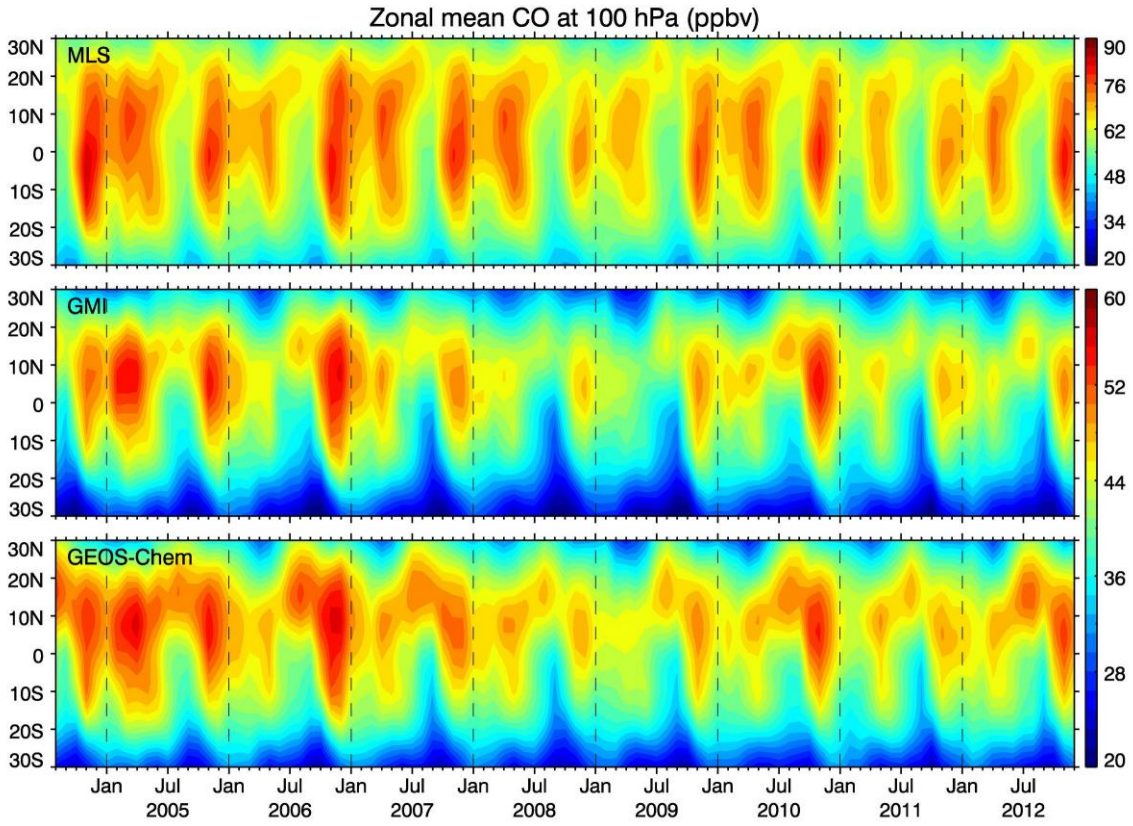

1067

1068 **Fig. 6.** As in Fig. 5, but for CO mixing ratio at 100 hPa.

1069

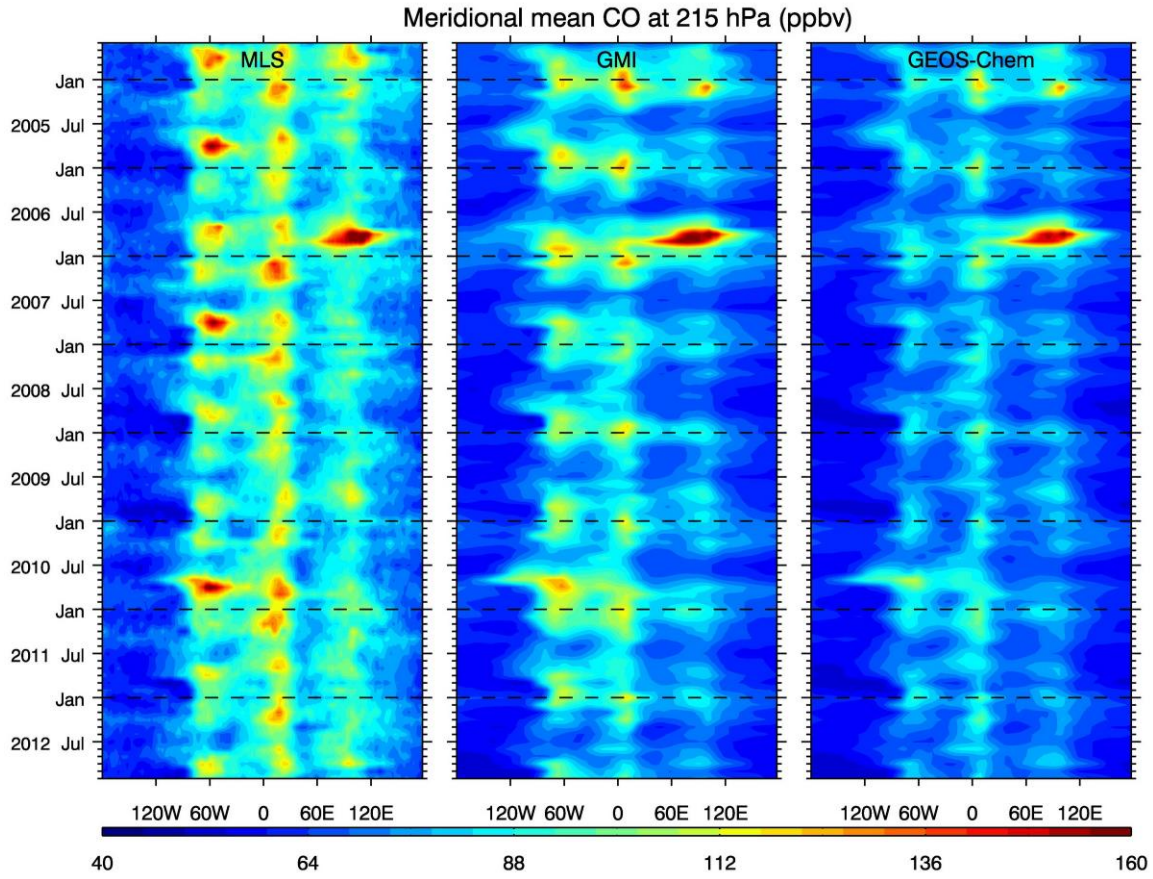

1070

1071 **Fig. 7.** Monthly variation of meridional mean (15°S–15°N) CO mixing ratio at 215 hPa

1072 for August 2004 – December 2012 from: (left) MLS V4 data; (middle) GMI model

1073 simulation with MLS AKs applied; (right) GEOS-Chem model simulation with MLS

1074 AKs applied.

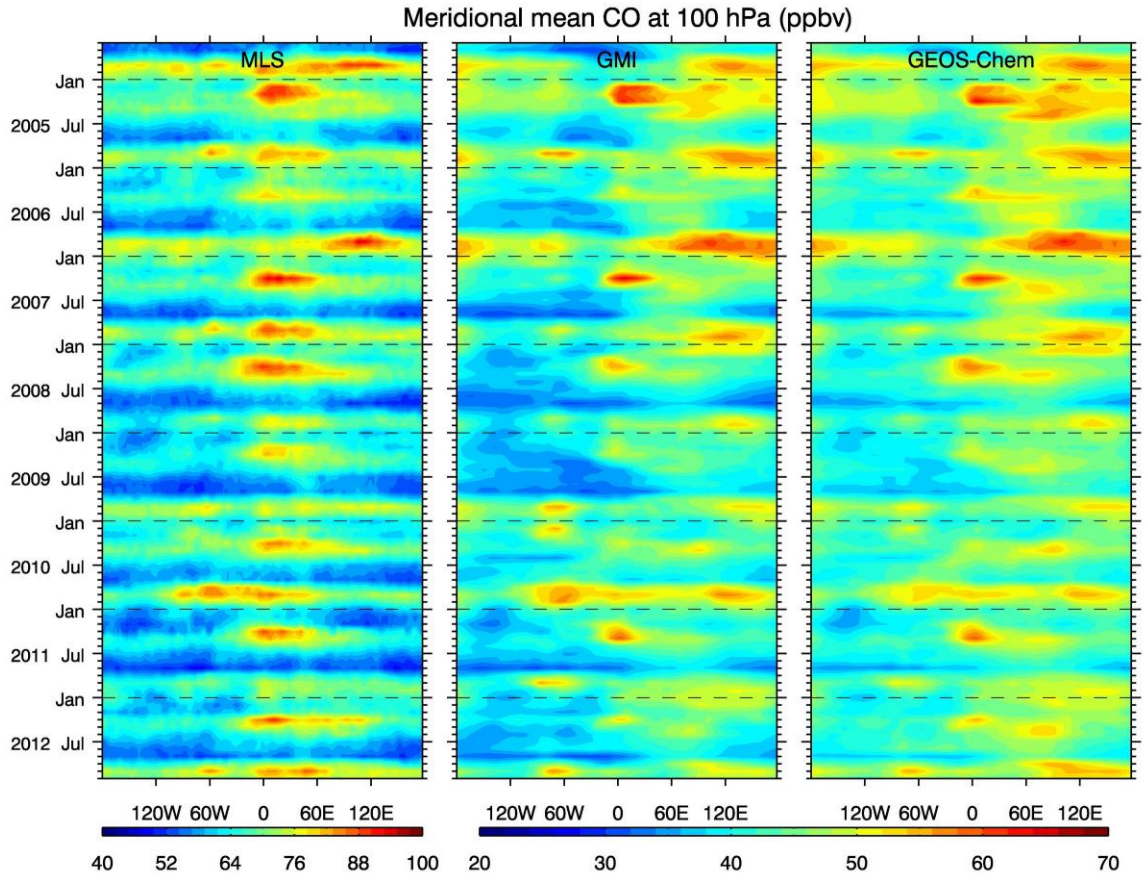

1075

1076 **Fig. 8.** As in Fig. 7, but for CO mixing ratio at 100 hPa.

1077

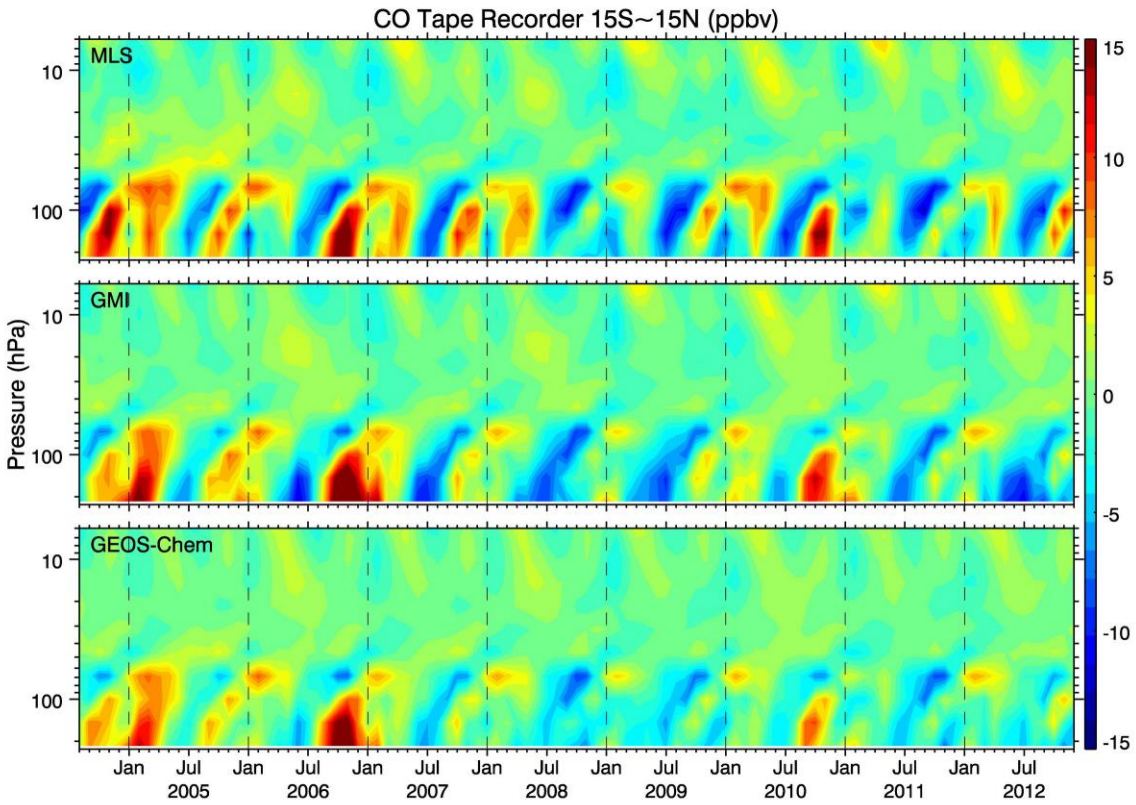

1078

1079 **Fig. 9.** Temporal variation of monthly mean CO deviations, zonally averaged over the
1080 tropics (15 ℃S–15 ℃N), vertically from 200 hPa to 50 hPa for August 2004 – December
1081 2012 from (top row) MLS V4 data; (middle row) GMI model simulation with MLS AKs
1082 applied; (bottom row) GEOS-Chem model simulation with MLS AKs applied. An 8-year
1083 mean (2005–2012) was subtracted from the monthly mean time series at each level for
1084 MLS data and the two models' simulations.

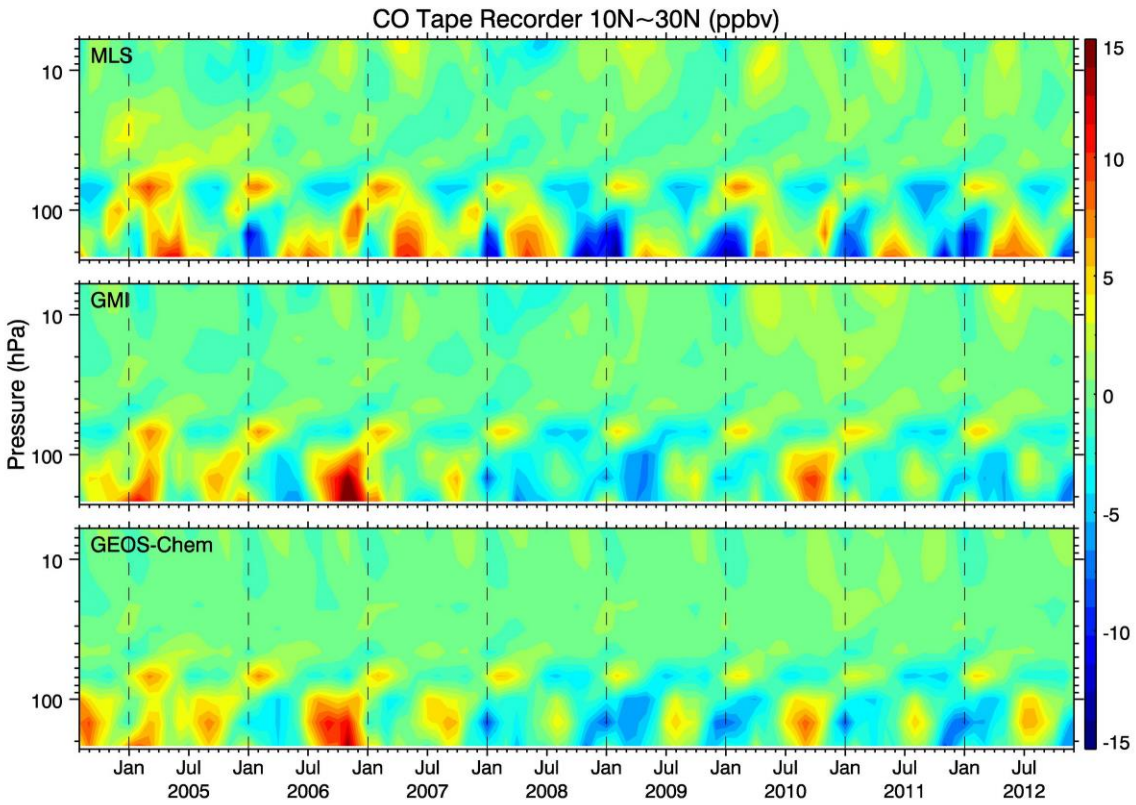

Fig. 10. As in Fig. 9, but over the northern subtropics (10 °–30 °N).

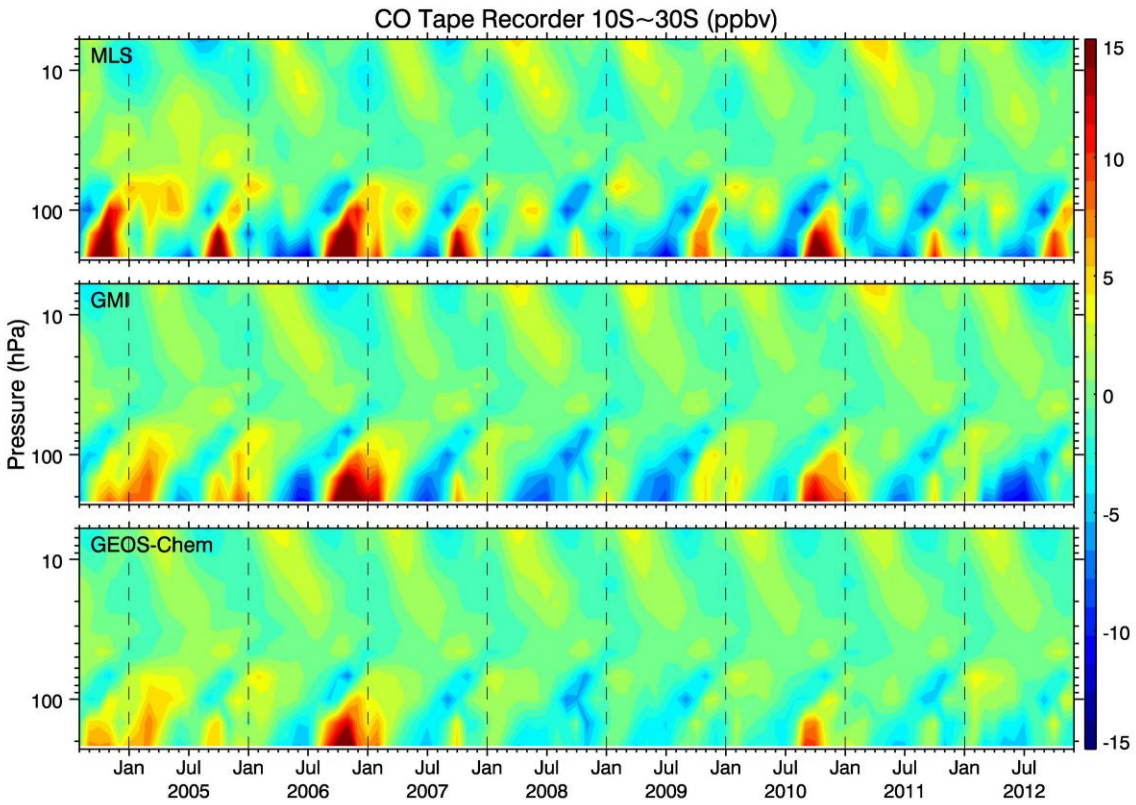

1088

1089 **Fig. 11.** As in Fig. 9, but over the southern subtropics (10 °–30 °S).

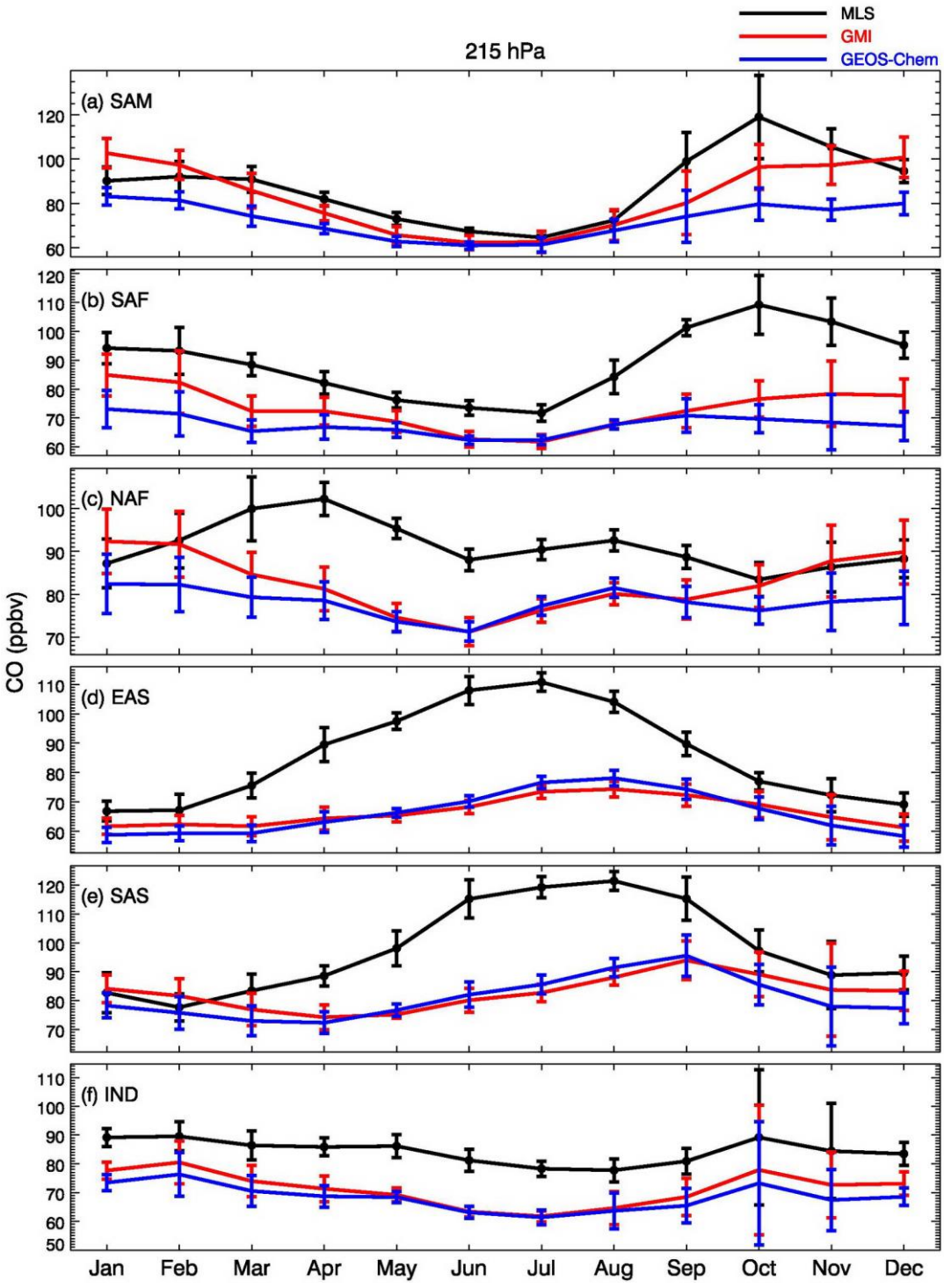

1090

1091 **Fig. 12.** Climatological (8-year) monthly mean of CO mixing ratio at 215 hPa from MLS

1092 V4 data (black line), GMI model simulation with MLS AKs applied (red line), and

1093 GEOS-Chem model simulation with MLS AKs applied (blue line) over the selected six

regions: (a) South America, (b) Southern Africa, (c) Northern Africa, (d) East Asia, (e) South Asia, and (f) Indonesia. The error bars indicate ±1 interannual standard deviation of the monthly mean CO from MLS observation and model simulations.

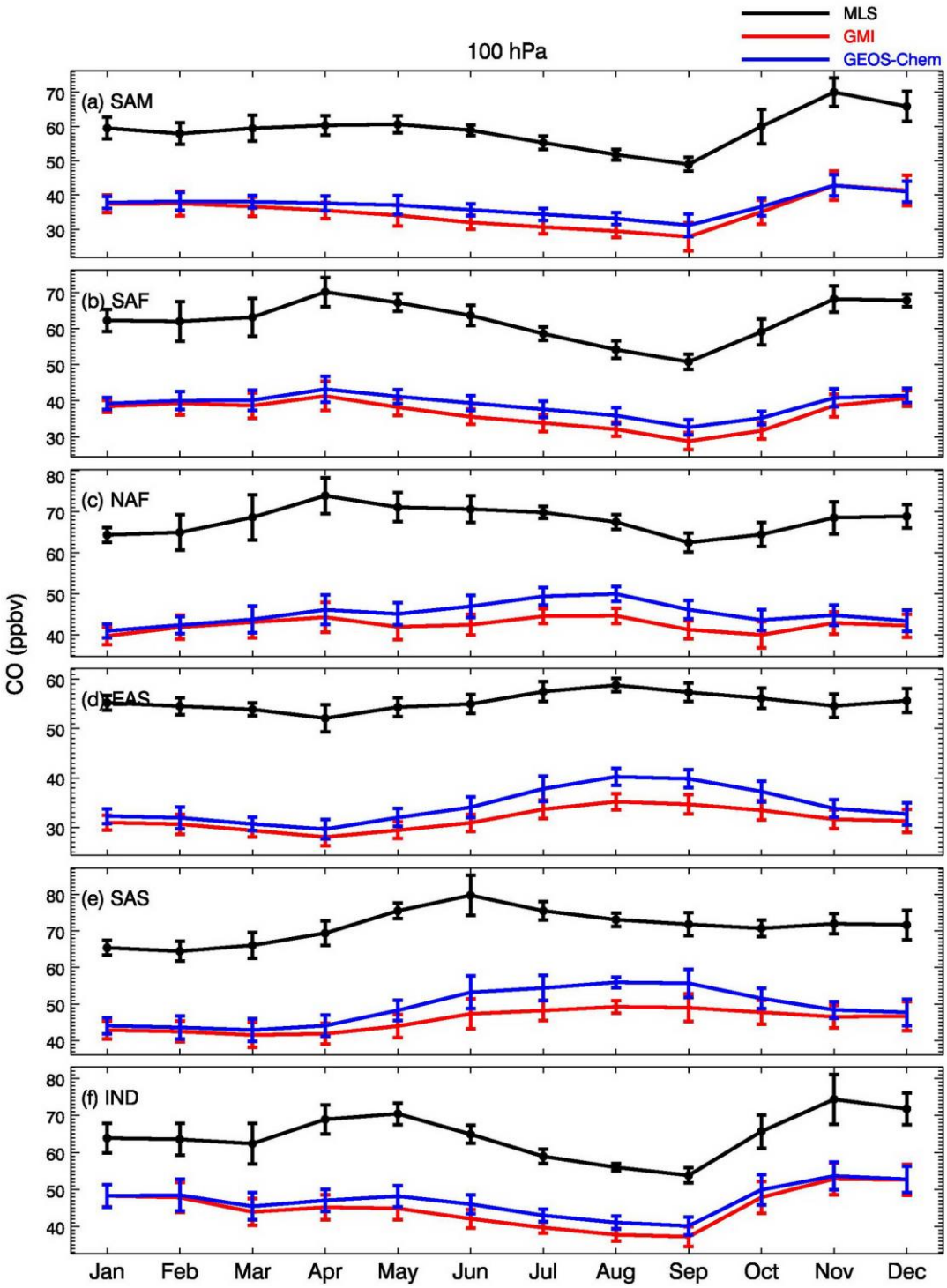

1098 **Fig. 13.** As in Fig. 12, but for CO mixing ratio at 100 hPa.

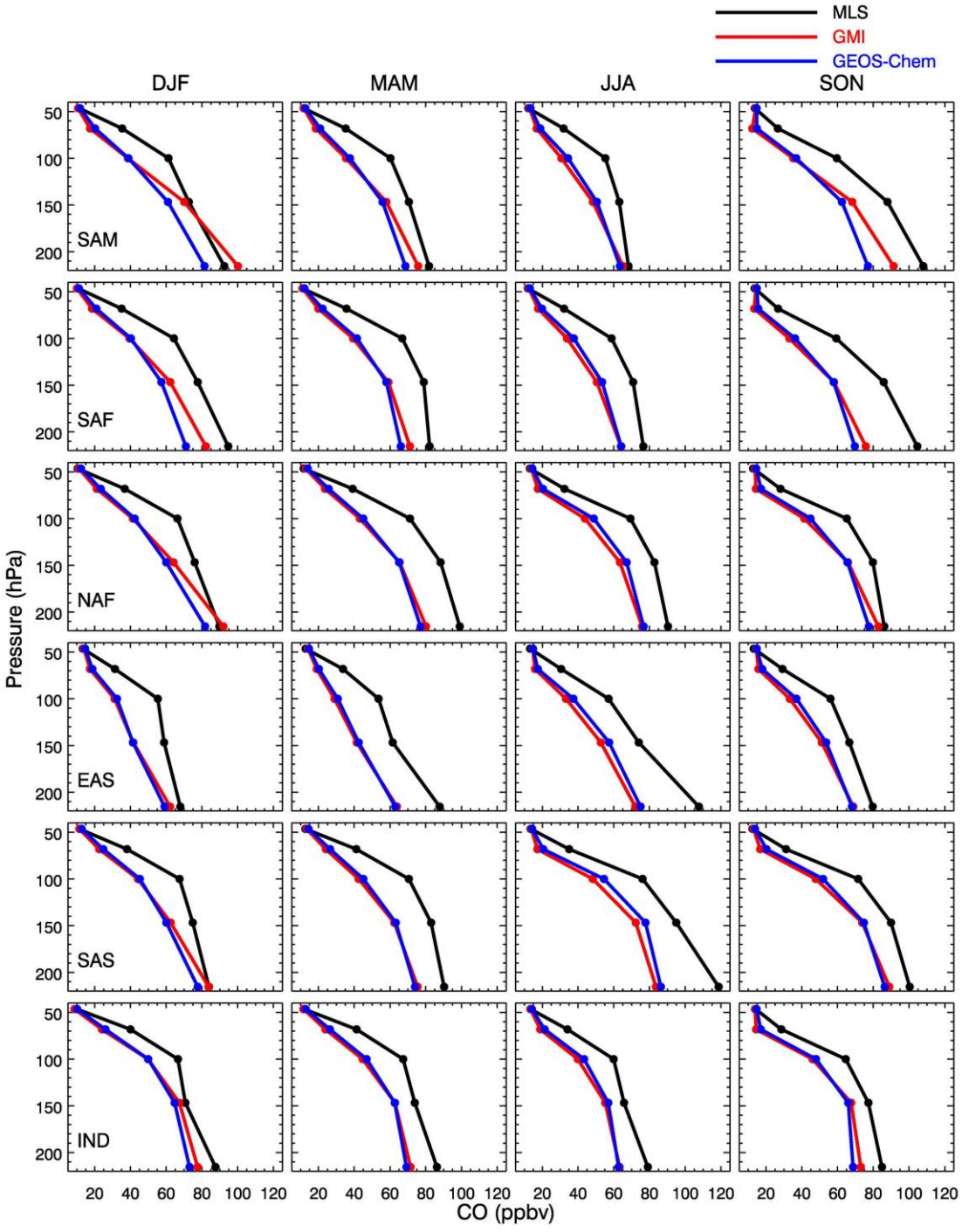

1099

1100 **Fig. 14.** Climatological (8-year) seasonal mean vertical profile of CO mixing ratio from
1101 MLS V4 data (black line), GMI model simulation with MLS AKs applied (red line), and
1102 GEOS-Chem model simulation with MLS AKs applied (blue line) over the selected six

regions: (top row) South America, (second row from top) Southern Africa, (third row from top) Northern Africa, (fourth row from top) East Asia, (fifth row from top) South Asia, and (bottom row) Indonesia.

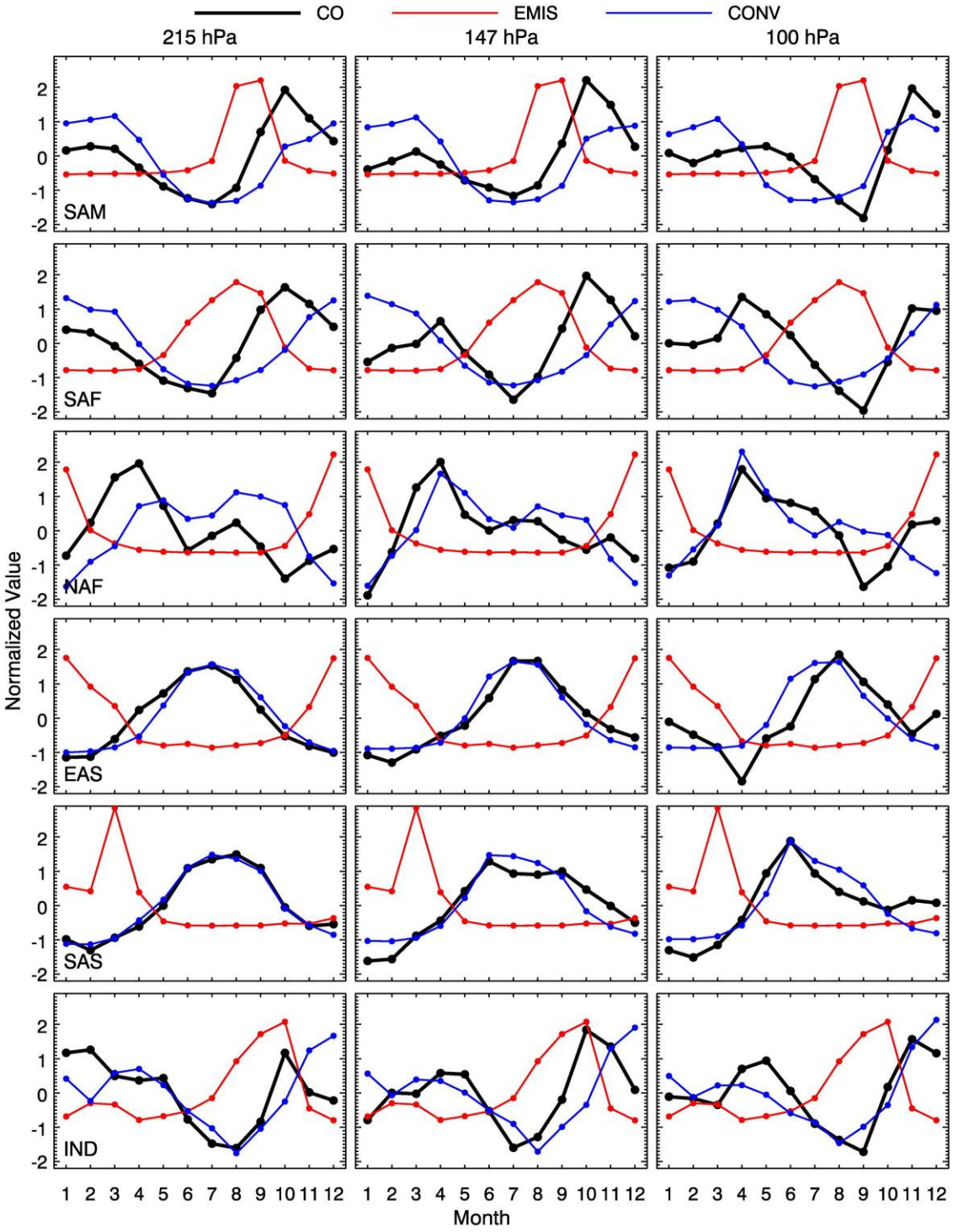

Fig. 15. Climatological monthly mean of surface CO emission from GMI model (red line), ice water content (blue line) and CO mixing ratio (black line) at 215 hPa (left column), 147 hPa (middle column), and 100 hPa (left column) from MLS observation over six regions: (top row) South America, (second row from top) Southern Africa, (third row from top) Northern Africa, (fourth row from top) East Asia, (fifth row from top) South Asia, and (bottom row) Indonesia. Each variable is normalized for comparison.

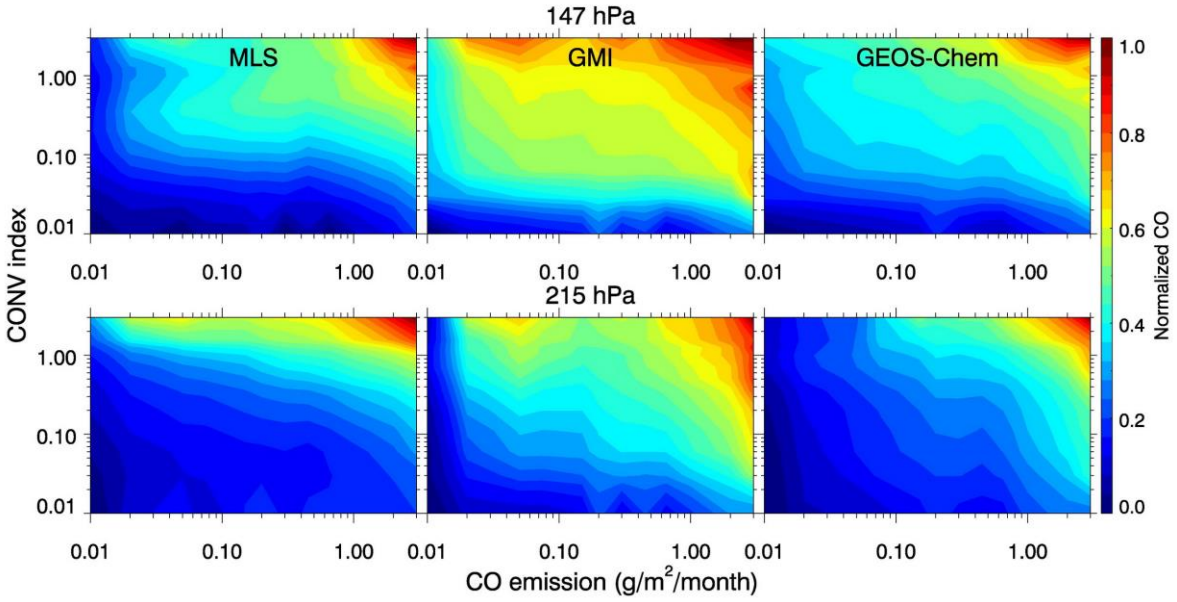

Fig. 16. Contour plots of normalized CO mixing ratio at 215 hPa (top row) and 147 hPa (bottom row) over the tropics (30°S–30°N) from MLS observation (left column), GMI model simulation (middle column), and GEOS-Chem model simulation (left column) binned according to the surface CO emission (x-axis) and convective index (y-axis) at the same pressure level. See text for more details.

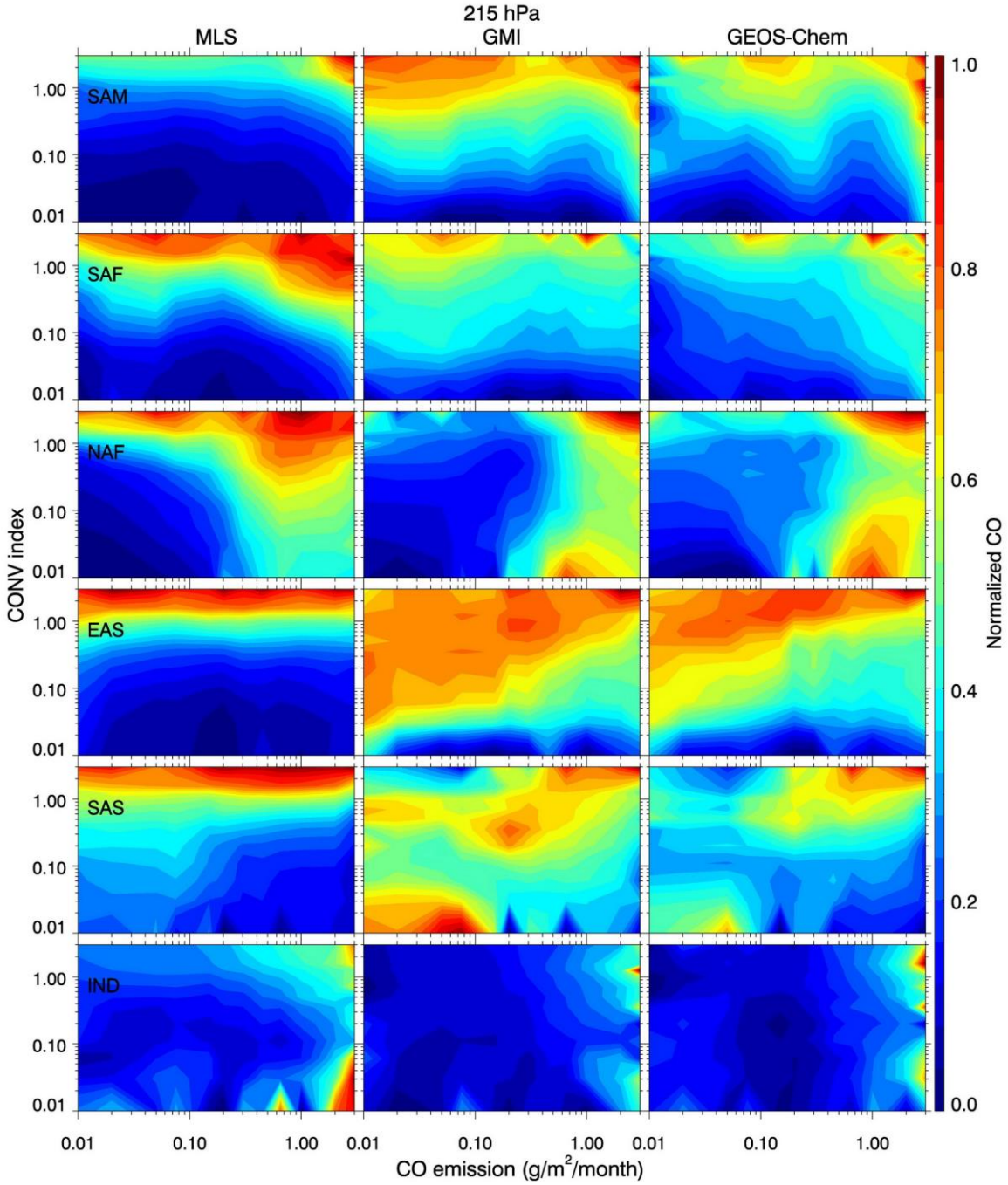

1119

1120 **Fig. 17.** Contour plots of normalized CO mixing ratio at 215 hPa over six regions: (top
1121 row) South America, (second row from top) Southern Africa, (third row from top)
1122 Northern Africa, (fourth row from top) East Asia, (fifth row from top) South Asia, and
1123 (bottom row) Indonesia, from MLS observation (left column), GMI model simulation
1124 (middle column), and GEOS-Chem model simulation (left column) binned according to

1125 the surface CO emission (x-axis) and convective index (y-axis) at the same pressure level.

1126 See text for more details.

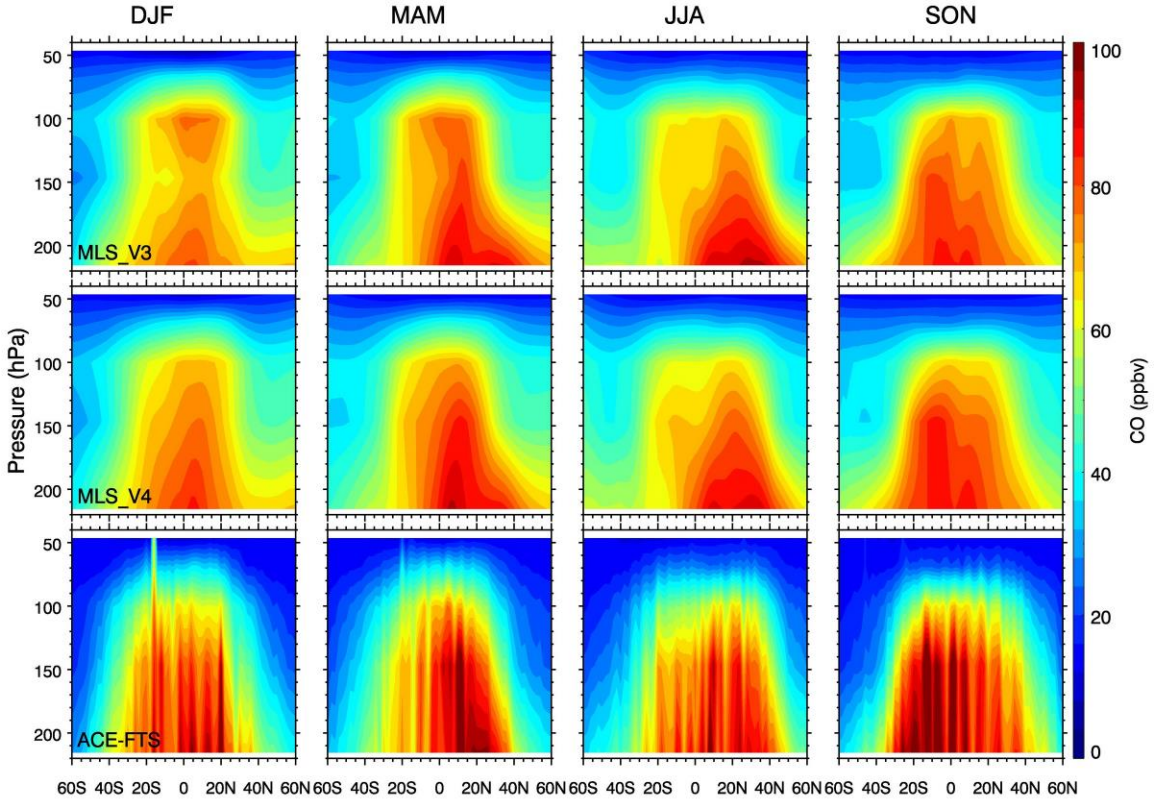

1127

1128 **Fig. A1.** Vertical distribution of zonal mean CO mixing ratio in the pressure-latitude

1129 cross-section during different seasons (DJF, MAM, JJA, and SON) from: (top row) MLS

1130 Version 3 CO data; (middle row) MLS Version 4 CO data; (bottom row) ACE-FTS CO

1131 data with MLS averaging kernels (AKs) applied.

1132

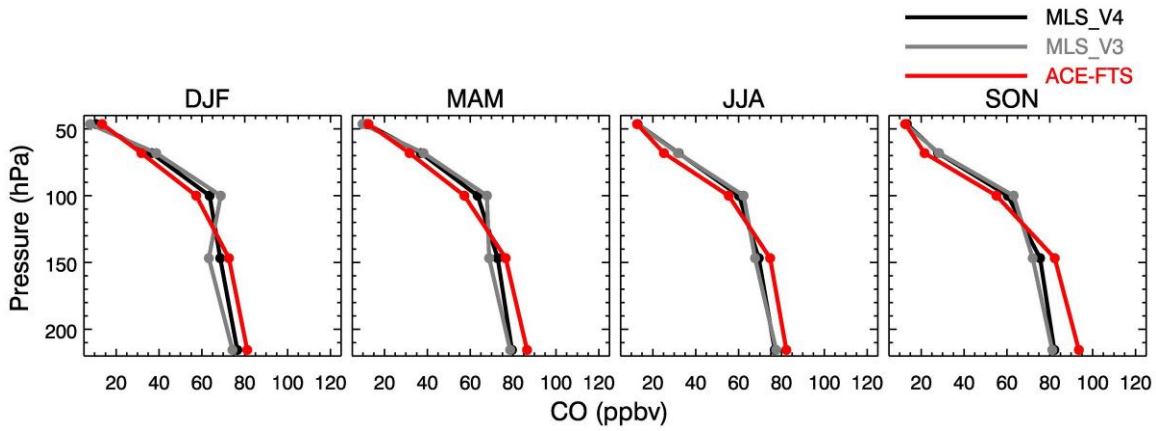

Fig. A2. Climatological (8-year) seasonal mean vertical profile of CO mixing ratio from MLS Version 4 CO data (black line), MLS Version 3 CO data (gray line), and ACE-FTS CO data with MLS AKs applied (red line) over the tropics (30 °S–30 °N).